

## Halo Properties and Mass Functions of Groups/Clusters from the DESI Legacy Imaging Surveys DR9

JIAQI WANG,<sup>1</sup> XIAOHU YANG,<sup>1,2</sup> JUN ZHANG,<sup>1</sup> HEKUN LI,<sup>1</sup> MATTHEW FONG,<sup>1</sup> HAOJIE XU,<sup>1</sup> MIN HE,<sup>1</sup> YIZHOU GU,<sup>1</sup>  
WENTAO LUO,<sup>3</sup> FUYU DONG,<sup>4</sup> YIRONG WANG,<sup>1</sup> QINGYANG LI,<sup>1</sup> ANTONIOS KATSIANIS,<sup>1</sup> HAORAN WANG,<sup>1</sup> ZHI SHEN,<sup>1</sup>  
PEDRO ALONSO,<sup>1</sup> CONG LIU,<sup>1</sup> YIQI HUANG,<sup>1</sup> AND ZHENJIE LIU<sup>1</sup>

<sup>1</sup>*Department of Astronomy, School of Physics and Astronomy, and Shanghai Key Laboratory for Particle Physics and Cosmology, Shanghai Jiao Tong University, Shanghai 200240, China*

<sup>2</sup>*Tsung-Dao Lee Institute and Key Laboratory for Particle Physics, Astrophysics and Cosmology, Ministry of Education, Shanghai Jiao Tong University, Shanghai 200240, China*

<sup>3</sup>*CAS Key Laboratory for Research in Galaxies and Cosmology, University of Science and Technology of China, Hefei, Anhui 230026, China*

<sup>4</sup>*School of Physics, Korea Institute for Advanced Study, 85 Heogiro, Dongdaemun-gu, Seoul, 02455, Republic of Korea*

Submitted to ApJ

### ABSTRACT

Based on a large group/cluster catalog recently constructed from the DESI Legacy Imaging Surveys DR9 using an extended halo-based group finder, we measure and model the group-galaxy weak lensing signals for groups/clusters in a few redshift bins within redshift range  $0.1 \leq z < 0.6$ . Here, the background shear signals are obtained based on the DECaLS survey shape catalog derived with the FOURIER\_QUAD method. We divide the lens samples into 5 equispaced redshift bins and 7 mass bins, which allow us to probe the redshift and mass dependence of the lensing signals and hence the resulting halo properties. In addition to these sample selections, we have also checked the signals around different group centers, e.g., brightest central galaxy (BCG), luminosity weighted center and number weighted center. We use a lensing model that includes off-centering to describe the lensing signals we measure for all mass and redshift bins. The results demonstrate that our model predictions for the halo masses, bias and concentrations are stable and self-consistent among different samples for different group centers. Taking advantage of the very large and complete sample of groups/clusters, as well as the reliable estimation of their halo masses, we provide measurements of the cumulative halo mass functions up to redshift  $z = 0.6$ , with a mass precision at  $0.03 \sim 0.09$  dex.

*Keywords:* Weak gravitational lensing; Observational cosmology; Galaxy clusters; Galaxy dark matter halos

### 1. INTRODUCTION

In the current scenario of structure formation and evolution, dark matter halos grow hierarchically from small perturbations in the initial density field (Lacey & Cole 1993). They are regarded as the building blocks of our Universe. The abundance, structure and spatial distribution of halos as a function of their host halo mass hold important information regarding the cosmological

parameters and structure formation theories (Press & Schechter 1974; White et al. 1993).

As dark matter halos are not directly observable, one needs to use fair mass/gravitational potential tracers to infer their mass and structure information. In literature, there are various kinds of scaling relations that have been established to infer halo masses in observations, e.g., using the X-ray luminosity of clusters (Pratt et al. 2009; Fujita & Aung 2019), the Sunyaev-Zeldovich effect of clusters (Sunyaev & Zeldovich 1972; Yang et al. 2022), the velocity dispersion of galaxy groups (Biviano et al. 2006; Munari et al. 2013; Elahi et al. 2018), satellite kinematics (van den Bosch et al. 2004; Li et al. 2019; Lange et al. 2019), the galaxy infall kinematics

(Zu & Weinberg 2013; Zu et al. 2014), and the abundance matching method (Yang et al. 2005; Yang et al. 2007; McGaugh & van Dokkum 2021), etc.

However, all the above methods to infer halo masses may either rely on a particular cosmology or need to assume the dynamical state of the tracers (Li et al. 2021), which are in general model dependent. A more direct way of detecting the halo mass and moreover the halo structure is using the gravitational lensing signals from large surveys. Using weak lensing to explore the halo properties has great advantages as it can directly measure the total mass distribution between the observer and the source (Bartelmann & Schneider 2001; Schneider 2005).

The halo mass function, which describes the number density and evolution of dark matter halos as a function of their mass, is one of the most important cosmological probes. During the past decades, great efforts were made to measure the halo mass around certain clusters, detected by the SZ effect (von der Linden et al. 2014; Hoekstra et al. 2015; Penna-Lima et al. 2017; Sereno et al. 2017) or their X-ray luminosity map (Prada et al. 2006; Gruen et al. 2014; Smith et al. 2015), using the weak lensing signals, so that halo mass scaling relations can be obtained and the abundance of the halos (halo mass function) at the high mass end can be measured. However, since the accuracy of weak lensing mass measurement of individual halos is limited by the quality and number density of background source images as well as their redshift distribution estimations, halo masses can only be reliably measured for a small number of the most massive clusters. On the other hand, through the stacking of weak lensing signals, one can measure the halo properties to much lower mass systems, e.g., from clusters to groups, and to isolated galaxies (Hirata & Seljak 2003; Mandelbaum et al. 2005, 2006; Zu et al. 2017; Medezinski et al. 2017; Luo et al. 2018). However, since it's difficult to quantify the completeness and obtain very accurate measurement of the abundance of the related lens systems, most of these studies still focus mainly on obtaining a weak lensing mass calibration for various halo mass indicators.

Recently, Yang et al. (2021, hereafter Y21) extended the halo-based group finder developed in Yang et al. (2005); Yang et al. (2007); Yang et al. (2012) so that it can deal with galaxy samples with photometric and spectroscopic redshifts simultaneously. Based on the DESI Legacy Imaging Surveys, they built the largest group catalog to date within redshift range  $0.0 < z \leq 1.0$ , and obtained halo mass estimation for each group by applying a total group luminosity ranking method. Thanks to this large and *complete* galaxy group catalog,

which gives important and reliable abundance information of the groups, we have the opportunity to obtain direct measurements of the halo mass functions in a relatively wide redshift range by applying the weak lensing stacking technique.

Based on the stacked weak lensing signals, in addition to the halo abundances (mass functions), one can also constrain other halo properties, including the concentrations and biases of halos, as a function of halo mass for different redshift bins. The concentration is a key quantity that characterizes the density structure of dark-matter halos, and can be used to trace the formation history of dark matter halos (e.g., Wechsler et al. 2002; Tasitsiomi et al. 2004; Zhao et al. 2009; Ludlow et al. 2013; Du et al. 2015; Xu et al. 2021). It depends on the halo mass, redshift, and cosmological parameters (e.g., Jing 2000; Prada et al. 2012). Halo bias  $b_h$  is defined as the ratio between the cluster halo density contrast  $\delta_h$  and the dark matter density contrast  $\delta_m$ . It traces the large scale environment of the halos, and is dependent on halo mass, and various secondary properties which were referred to as the ‘assembly bias’ (e.g., Gao et al. 2005; Gao & White 2007; Xu et al. 2021) and cosmology (e.g., Jing et al. 1998; Sheth et al. 2001; Seljak & Warren 2004; Tinker et al. 2010). Given those dependencies, useful cosmological information can be derived using one or a combination of these measurements (see Ingoglia et al. 2022, for a recent attempt).

To accurately measure the weak lensing signals, one needs both high quality imaging of background galaxies and accurate image processing procedures. Many groups have developed image processing pipelines devoted to improving the accuracy of shape measurement (Kaiser et al. 1995; Bertin & Arnouts 1996; Maoli et al. 2000; Rhodes et al. 2000; Van Waerbeke et al. 2001; Bernstein & Jarvis 2002; Bridle et al. 2002; Refregier 2003; Bacon & Taylor 2003; Hirata & Seljak 2003; Heymans et al. 2005; Miller et al. 2007; Kitching et al. 2008; Zhang 2010, 2011; Bernstein & Armstrong 2014; Zhang et al. 2015; Zhang 2016; Luo et al. 2017). Among these, the FOURIER\_QUAD method developed by Zhang et al. (2015) and Zhang et al. (2019) is a particularly efficient one. It uses the image moments in the Fourier Domain to recover the shear signal, with rigorous (model independent) treatments of the point distribution function (PSF) effect, the background and Poisson noise. It runs with a very high speed ( $\sim 10^{-3}$  CPU\*sec/galaxy) (see Mandelbaum et al. 2015, for the performance comparison of a variety of pipelines), quite suitable for large scale weak lensing measurement. Observationally, the DESI Legacy Imaging Surveys (Dey et al. 2019) provides the currently largest sky coverage of extragalac-

tic sources with good imaging qualities in three optical bands ( $g, r, z$ ). One of DESI's subprograms, the Dark Energy Camera Legacy Survey (DECaLS) images the full DESI equatorial footprint. It provides increased depth and excellent seeing, and has more than a hundred million galaxies in 3 bands, thus provides an ideal data set for weak lensing studies.

In this study, we combine the large group and shear catalogs, both constructed from the DESI Legacy Imaging Surveys, to carry out our investigations. The main purpose is to obtain a set of reliable measurements of the (cumulative) halo mass functions in a few redshift bins up to redshift  $z = 0.6$ . Meanwhile, we will also provide the observational constraints on the concentration - halo mass and bias - halo mass relations in a few redshift bins. These sets of measurements can be used in further studies to probe the structure formation theory and cosmological parameters. The structure of this paper is organized as follows. We first describe the data sets used in this study, including the lens samples and the shear catalogs in §2. The model to describe the lensing signals is presented in §3. The general halo properties obtained from fitting the lensing signals are given in §4. We provide our estimation of the cumulative halo mass functions in §5. Finally we summarize our results in §6. Throughout this paper, we assume a  $\Lambda$ CDM cosmology with parameter values from the latest Planck Collaboration analysis (Planck Collaboration et al. 2020, hereafter Planck18):  $\Omega_m = 0.315$ ,  $\Omega_\Lambda = 0.685$ ,  $\sigma_8 = 0.811$ ,  $n_s = 0.965$  and  $h = 0.674$ . All distances are in comoving units of  $h^{-1}$ Mpc. The unit of projected surface mass density  $\Sigma$  and density contrast  $\Delta\Sigma$  is  $hM_\odot/\text{pc}^2$ . In this work, halos are defined to have 180 times the mean background density  $M_{180m}$ .

## 2. OBSERVATIONAL DATA

In this section we describe the construction of our lens samples and the source shear catalogs.

### 2.1. Lens samples

We use the group catalog recently constructed by Y21 from the DESI legacy imaging surveys (now updated to DR9) using an adaptive halo-based group finder for galaxies with either photometric or spectroscopic redshifts<sup>1</sup>.

As demonstrated in Y21, using mock galaxy redshift surveys, the group finder can reliably detect most of the groups, especially with mass  $\gtrsim 10^{13.0} h^{-1}M_\odot$ , where the group *purity* is larger than 90%. That means

more than 90% of the detected groups are the original true groups in simulations. The halo mass assigned to each group (hereafter, the group mass,  $M_G$ ) has an uncertainty of about 0.2 dex at the high mass end ( $\gtrsim 10^{14.0} h^{-1}M_\odot$ ), increasing to 0.4 dex at the mass ( $\sim 10^{12.3} h^{-1}M_\odot$ ) and then decreasing to 0.3 dex at low mass end ( $\sim 10^{11.6} h^{-1}M_\odot$ ). As the main purpose of this study is to obtain an accurate measure of the halo mass function, where the group *purity* is most important, we select groups/clusters with mass  $M_G > 10^{13} h^{-1}M_\odot$ . Note that, as the group masses in the catalog are obtained via a halo abundance matching method,  $M_G$  in general can be regarded as a measure for the rank-order in the total group luminosity. Here we use group mass rather than the total group luminosity as our rank-order group sample selection criteria, as the groups are extracted from a flux-limited sample and the total group luminosity may suffer from different incompleteness cuts. In addition, in order to assure that groups have sufficient richness, we only use groups in the redshift ranging from  $0.1 \leq z < 0.6$ . We divide all the groups/clusters with the above criteria into 5 redshift bins and 7 mass bins, which results in a total of 35 lens samples. The selection criteria and the number of groups in these lens samples are illustrated in Fig. 1. The redshift and mass bins are divided by the solid lines in the figure, and the number of groups in each bin is given in each block. Overall, the vast majority of groups in our 35 lens samples contain at least two members, only a very small fraction of groups at high redshift and low mass bins contain only one member galaxy.

Once these lens samples are selected, we need to determine the choice of group centers for stacking the lensing signals. As pointed out in Luo et al. (2018), the brightest central galaxy (BCG) is a better tracer of the halo center when compared to the luminosity weighted center (LWC) and the number weighted center (NWC). However, as we will outline later in Section 3.2, since we have taken potential off-centering effect into account in our lensing models, in general, we can use the extracted halo information from different sets of halo center indicators for cross checks. Thus, we decide to measure the group-galaxy lensing signals around all these three types of group/cluster center indicators. We take the BCG as our fiducial case, and the other two as reference cases.

### 2.2. The shear catalog

Our shear catalog is constructed using the imaging data of the DECaLS DR8 (Dey et al. 2019). The survey uses the Dark Energy Camera (DECam) installed on the Blanco 4m telescope. It is designed to target sources for the DESI program in the North Galactic

<sup>1</sup> see <https://gax.sjtu.edu.cn/data/DESI.html>

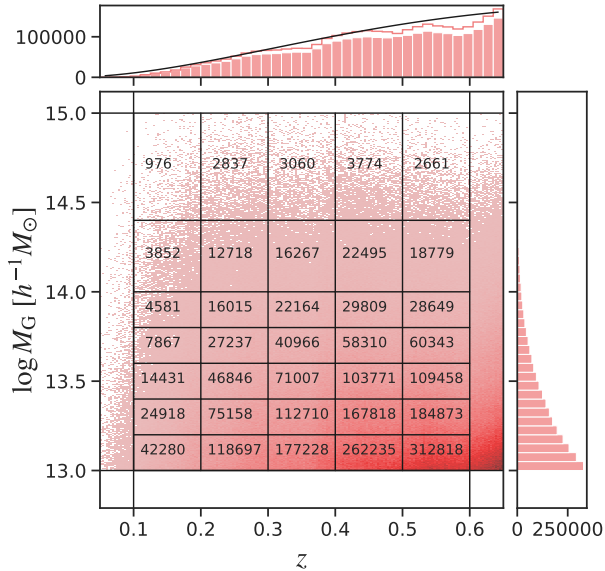


**Figure 1.** The distribution of group/cluster sample in the redshift and mass proxy space. The  $x$ -axis is the redshift and the  $y$ -axis is the group mass. The black solid lines label out thresholds of our redshift and mass bins. The numbers in each block are the number of groups. The top and right panels show the number distributions of groups using 1D shaded histograms according to the redshift and group mass, respectively. In the top panel, we also provide the number distribution of groups after completeness correction (see Eq. 14) using a red histogram and the theoretical prediction of the number distribution of halos with mass larger than  $10^{13} h^{-1} M_{\odot}$  under Planck18 cosmology using a black line (Tinker et al. 2008).

Cap region at  $\text{Dec} \leq 32^{\circ}$  and the South Galactic Cap region at  $\text{Dec} \geq -34^{\circ}$ . The images are taken in  $g, r, z$  three bands. The total sky coverage by the images is more than  $10000 \text{ deg}^2$ . Our source galaxy catalog is taken from Zou et al. (2019), with photometric redshifts of galaxies updated using those obtained by Zhou et al. (2021) with a machine learning algorithm, with a typical redshift error  $z_{\text{err}}/(1+z) = 0.02 \sim 0.03$  in redshift range  $0.4 \leq z < 0.9$  (see Fig. 4 in Zhou et al. (2021)).

Shear catalogs are constructed from the DECaLS DR8 using the FOURIER\_QUAD (FQ) method (Zhang 2008; Zhang et al. 2022; Mandelbaum et al. 2015). FQ is a moment-based method. Its shear estimators are defined with the multipole moments of the 2D galaxy power spectrum, which can correct for the effect of Point Spread Function model-independently. The effects due to the background noise and the Poisson noise can also be removed rigorously in statistics. The method has been tested under general observing conditions to a very low Signal-to-Noise Ratio (SNR) of the source image (SNR < 10) (Zhang et al. 2015). The full image process-

ing pipeline based on the FQ method has been developed and applied on the CFHTLenS (Heymans et al. 2012; Erben et al. 2013) and the DECaLS data. In both cases, the resulting shear catalogs can successfully recover the small optical field distortion signals ( $\sim 1-5 \times 10^{-3}$ ) that are originally derived from the astrometric calibrations, demonstrating its robustness in practice (Zhang et al. 2019; Wang et al. 2021). In the development of the FQ pipeline, we have carefully studied the source selection effect due to the inevitable incompleteness of sources at the faint end (Li et al. 2021), and also included an algorithm to avoid the systematic errors (additive) due to the presence of the geometric boundaries (CCD edges, bad columns, etc. Wang et al. 2021).

An interesting feature of FQ is that it tolerates the existence of very poorly resolved images or even point sources in the galaxy samples. This property is particularly important for our processing of the DECaLS data, as the typically full width at half maximum (FWHM) of the PSF is about 1.4-1.5 arcsec, much larger than those of other weak lensing surveys. Overall, our FQ image processing pipeline for the DECaLS data is very similar to that of Zhang et al. (2019), except for some details regarding the PSF reconstruction (see Zhang et al. 2022, for the details of the construction of DECaLS DR8 shear catalog).

Since FQ works on individual exposures, in our DECaLS shear catalog, images of the same galaxy on different exposures contribute independent shear estimators. As the  $g$ -band image quality is not as good as the  $r$  and  $z$ -bands, we decide to use the  $r$  and  $z$  band shear catalogs for our calculations in this paper. Note that the multiple (multi-band) shear estimators from each galaxy are used together in our measurement of this work. On average, the catalogs contain results from more than 10 source images per square arcmin, with a median redshift at around 0.55.

### 3. ESD MEASUREMENT AND MODELING

In this section, we provide our measurement and modeling of the excess surface densities (ESDs) around our lens samples.

#### 3.1. ESD Measurement

The weak lensing signal around foreground galaxy groups/clusters is related to the foreground density profile as:

$$\Delta\Sigma(r) = \gamma_t(r) \Sigma_c, \quad (1)$$

in which  $\Delta\Sigma(r)$  is the excess surface density in comoving units,  $\gamma_t(r)$  is the tangential shear, and  $\Sigma_c$  is the critical surface density defined as:

$$\Sigma_c = \frac{c^2}{4\pi G} \frac{D_s}{D_l D_{ls} (1+z_l)^2}, \quad (2)$$

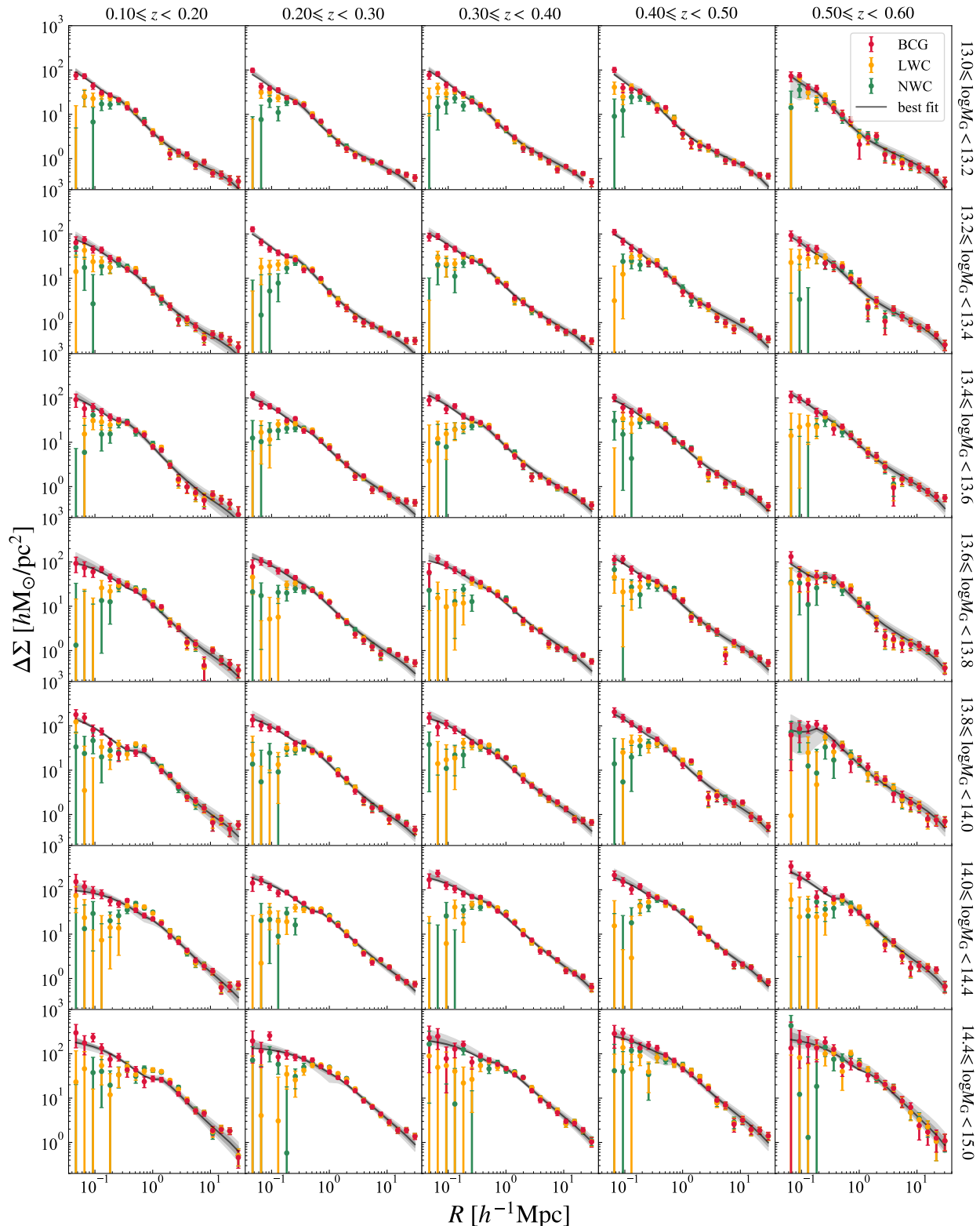


**Figure 2.** The excess surface density of DESI Legacy Imaging Surveys DR9 lens samples in different redshift and mass bins as indicated in different columns and rows. In each panel, we compare results for three different group center indicators. The red points represent results for the BCG group center, orange for the LWC and green for the NWC. We can see that BCG performs the best as a center indicator. The solid line in each panel shows the best-fit model (Eq. 7) of the ESD for BCG centroid. The dark and light grey shaded regions represent the 68 and 95 confidence regions of the ESD fitting results respectively.

where  $D_s$ ,  $D_l$  and  $D_{ls}$  are the angular diameter distances of the source, the lens, and between the source and the lens,  $c$  is the light speed and  $G$  is the gravitational constant.  $z_l$  refers to the redshift of the lens, and the factor  $(1 + z_l)^2$  is included to account for the conversion from the physical units to the comoving ones.

In our measurement, the ESD around different lens are stacked using the PDF-symmetrization (PDF\_SYM) method within each sample. To approach the lower bound of the statistical uncertainty, i.e. the Cramer-Rao Bound, Zhang et al. (2017) (Z17 hereafter) proposed the PDF\_SYM method, which can maximally utilize the ensemble information of the shear estimators based on the distribution function. Instead of taking the weighted average of the shear estimators as what is usually done, the idea of Z17 is to find the shear signal that can best symmetrize the PDF of the corresponding shear estimators. For example, for an underlying shear signal  $g_1$ , its best estimate  $\hat{g}_1$  can be found by symmetrizing the PDF of the quantity  $G_1 - \hat{g}_1(N + U)$ , in which  $G_1$  is the shear estimator along the specified direction,  $N$  is the normalization factor, and  $U$  is a spin-4 quantity defined in Z17 to account for the parity symmetry. Note that the value of  $U$  is also dependent on the direction of the coordinates.

For the ESD measurement, the operation is quite straightforward. For a given foreground lens sample at  $z_l$ , instead of shear along a specified direction  $\hat{g}_1$ , we directly look for the value of the excess surface density  $\widehat{\Delta\Sigma}$  that can best symmetrize the PDF of the following quantity:

$$G_t(z_s) - \frac{\widehat{\Delta\Sigma}}{\Sigma_c(z_l, z_s)} \cdot (N + U_t)(z_s), \quad (3)$$

where  $z_s$  stands for the source redshift, while  $G_t$  and  $U_t$  are all defined in the tangential direction. The PDF is made of the quantities defined in Eq. 3 from all the background galaxies in a given radius range of interest. In doing so, we properly take into account the contribution from different background redshifts. Simulations regarding the verifications of the PDF\_SYM method on the measurement of the excess surface density will be reported in a separate work (Li et al., in preparation), in which we also discuss about the effects related to photo- $z$  errors.

In this work, to avoid the dilution effect by foreground galaxies, we only use sources with redshift  $z_s > z_l + \Delta z$ , with  $\Delta z = 0.2$ . The photo- $z$  errors of the background sources cause the uncertainty of  $\Sigma_c$ , which in turn leads to bias in the ESD signal, making it slightly higher/lower in the lowest/highest redshift bin of our lens sample. This bias, which ranges from almost zero to about 2%,

are corrected using the redshift PDF (fully discussed in Li et al., in preparation). The covariance matrix in this work is computed using 400 jackknife samples.

Using the above method, we obtain the ESDs around  $5 \times 7$  lens samples with three types of group center indicators. The dots with error bars shown in Fig. 2 are the measured ESDs, where different colors correspond to different group center indicators. Considering the signal-to-noise ratios of the ESD measurements, we provide one less data point on the smallest scale for lens samples in the two high redshift bins than the three low redshift bins. In these lens samples, the ESD amplitudes increase more quickly for samples with higher group mass than for samples with higher redshift. There are no significant differences for ESDs around different centers at large scales. At small scales ( $\leq 0.5 h^{-1}\text{Mpc}$ ), ESDs of samples using BCG as center indicators keep rising with decreasing central distance, while other two central indicators tend to decrease. The signal-to-noise ratio is low at small scales, especially for the samples using LWC or NWC centroid, due to the decreasing lens-background pairs and the possible large offsets.

### 3.2. ESD Modeling

Here we describe the ESD model we use to extract the halo properties. Theoretically, the ESD around a lens sample is related to the line-of-sight projection of the group-matter cross correlation function,

$$\xi_{\text{gm}}(r) = \langle \delta_{\text{g}}(\mathbf{x})\delta_{\text{m}}(\mathbf{x} + \mathbf{r}) \rangle, \quad (4)$$

so that (Yang et al. 2006; van den Bosch et al. 2013, e.g.),

$$\Sigma(R) = 2\bar{\rho} \int_R^\infty [1 + \xi_{\text{gm}}(r)] \frac{r dr}{\sqrt{r^2 - R^2}}, \quad (5)$$

and

$$\Sigma(\leq R) = \frac{4\bar{\rho}}{R^2} \int_0^R y dy \int_y^\infty [1 + \xi_{\text{gm}}(r)] \frac{r dr}{\sqrt{r^2 - y^2}}, \quad (6)$$

where  $\bar{\rho}$  is the average background matter density of the Universe. In general, from the weak lensing shear catalogs, we are measuring the ESDs around the lens systems, i.e.,  $\Delta\Sigma(R) = \Sigma(\leq R) - \Sigma(R)$ . Following Luo et al. (2018, hereafter L18), our ESD model contains three components:

$$\Delta\Sigma(R) = \Delta\Sigma_*(R) + \Delta\Sigma_{1\text{h}}(R) + \Delta\Sigma_{2\text{h}}(R), \quad (7)$$

where they correspond to, from small to large scales, the contributions of (1) the stellar mass of the lens galaxy  $\Delta\Sigma_*(R)$ , if BCG is used to indicate the group center; (2) the 1-halo term contribution from the host halo mass

taking into account the off-centering effect  $\Delta\Sigma_{1h}(R)$ ; and (3) the projected two halo term  $\Delta\Sigma_{2h}(R)$ , respectively.

As demonstrated in L18, stellar contribution is significant at scales smaller than  $50 h^{-1}\text{kpc}$ , then on  $50 h^{-1}\text{kpc} \sim 5 h^{-1}\text{Mpc}$  scales the host halo contributes most of the ESDs. The 2-halo term contribution is then important at scales larger than a few virial radii. As we have obtained the ESD measurements for our lens samples over much larger scales, we can obtain both the 1-halo and the 2-halo term properties of dark matter halos in this study. Below we present each term of our ESD model in Eq. 7. Note that only small changes are made with respect to the one provided in L18.

The first term in Eq.7 is contributed by the stellar mass of the lens galaxy. As pointed out in Johnston et al. (2007) and George et al. (2012), the stellar mass component can be treated as a point mass, and the related ESD can be modelled as,

$$\Delta\Sigma_*(R) = \frac{M_*}{\pi R^2}, \quad (8)$$

where  $M_*$  is the stellar mass of candidate BCGs in consideration, obtained using the  $K$ -correction software of Blanton & Roweis (2007, v4.3) by applying to the BCG 5 band apparent magnitudes. We only model the contribution of the stellar component (using eq. 7) for the BCG group center indicator, using the average stellar mass of all BCGs in the stack.

The second term in Eq.7 is the 1-halo term contribution. Here we divide the ESDs into two components, one for the halo center and the other for an off-centering situation,

$$\Delta\Sigma_{1h}(R) = f_{\text{cen}}\Delta\Sigma_{\text{NFW}}(R) + (1 - f_{\text{cen}})\Delta\Sigma_{\text{off}}(R), \quad (9)$$

where  $f_{\text{cen}}$  is the fraction of groups that do not suffer from off-centering effect,  $\Delta\Sigma_{\text{NFW}}(R)$  is ESD of the halo assuming an NFW profile (see Eq. A2). For the off-centering halo contribution,  $\Delta\Sigma_{\text{off}}(R)$ , according to Yang et al. (2006), the projected surface density for a galaxy with a projected off-center distance  $R_{\text{off}}$  from the NFW halo center, can be described by  $\Sigma_{\text{off}}(R|M_h, c, R_{\text{off}})$  (Eq. A4). Here,  $M_h$  and  $c$  are the mass and concentration obtained by weak lensing that correspond to  $M_{180\text{m}}$ . Here, we adopt the model proposed by Johnston et al. (2007) to take into account the off-centering effect,

$$P(R_{\text{off}}) = \frac{R_{\text{off}}}{R_{\text{sig}}^2} \exp(-0.5(R_{\text{off}}/R_{\text{sig}})^2), \quad (10)$$

where  $R_{\text{sig}}$  is the dispersion of  $P(R_{\text{off}})$ . The resulting projected density profile is the convolution between the

$P(R_{\text{off}})$  and the  $\Sigma_{\text{off}}(R|M_h, c, R_{\text{off}})$ ,

$$\Sigma_{\text{off}}(R|M_h, c, R_{\text{sig}}) = \int dR_{\text{off}} P(R_{\text{off}}) \Sigma_{\text{off}}(R|M_h, c, R_{\text{off}}). \quad (11)$$

Finally, the last term in Eq. 7 is contributed by the 2-halo term. The contribution from the projected mass density field outside the halo,  $\Delta\Sigma_{2h}(R)$ , can be calculated from the halo-mass cross correlation functions using Eqs. 5 and 6. Here we adopt the model proposed in van den Bosch et al. (2013) to describe the 2-halo term cross correlation function,

$$\xi_{\text{gm},2h}(r) = b_h \zeta(r, z) f_{\text{exc}}(r) \xi_{\text{mm}}(r), \quad (12)$$

where  $\xi_{\text{mm}}(r)$  is the auto correlation function of dark matter calculated from the nonlinear power spectrum (Smith et al. 2003, e.g.),  $f_{\text{exc}}(r)$  is to characterize the halo exclusion effect (see Eq. A5),  $\zeta(r, z)$  is a function used to take into account the radial dependence of the halo bias (see Eq. A7), and  $b_h$  is the last free parameter in our ESD modeling describing the bias of the dark matter halos.

In total, we have five free parameters in our ESD model,  $M_h, c, f_{\text{cen}}, R_{\text{sig}}$  and  $b_h$  for our ESD measurements for all group centers. Below we outline the processes we use to constrain the model parameters.

### 3.3. Model fitting

For each of our 35 lens samples, we use a Gaussian likelihood function with covariance matrix built from 400 jackknife samplings,

$$\ln \mathcal{L}(\mathbf{X}|\Theta) = -0.5((\mathbf{X} - \mathbf{ESD}_m)^T C^{-1}(\mathbf{X} - \mathbf{ESD}_m)), \quad (13)$$

where  $\mathbf{X}$  is the ESD observational measurement data vector,  $\mathbf{ESD}_m$  is the model and  $C^{-1}$  is the inverse of the covariance matrix.  $\Theta$  denotes the parameters in the ESD model. In order to minimize the prior influence, we use broad flat priors for all of the model parameters. We set the logarithm of halo mass  $\log M_h$  to be within (12.0, 16.0), concentration range (1.0, 20.0), central fraction  $f_{\text{cen}}$  to be within (0.0, 1.0),  $R_{\text{sig}}/r_{180\text{m}}$  range (0.0, 1.0) and bias  $b_h$  range (0.3, 10.0). The halo parameters are estimated by the Markov Chain Monte Carlo fitting method using the emcee package<sup>2</sup> (Foreman-Mackey et al. 2013). For each of the lens samples, we adopt an ensemble sampler with 72 walkers over a chain of 720000 steps, where the first 72000 steps are discarded in our subsequent analysis. From each of the final chain,

<sup>2</sup> <https://emcee.readthedocs.io/en/stable>

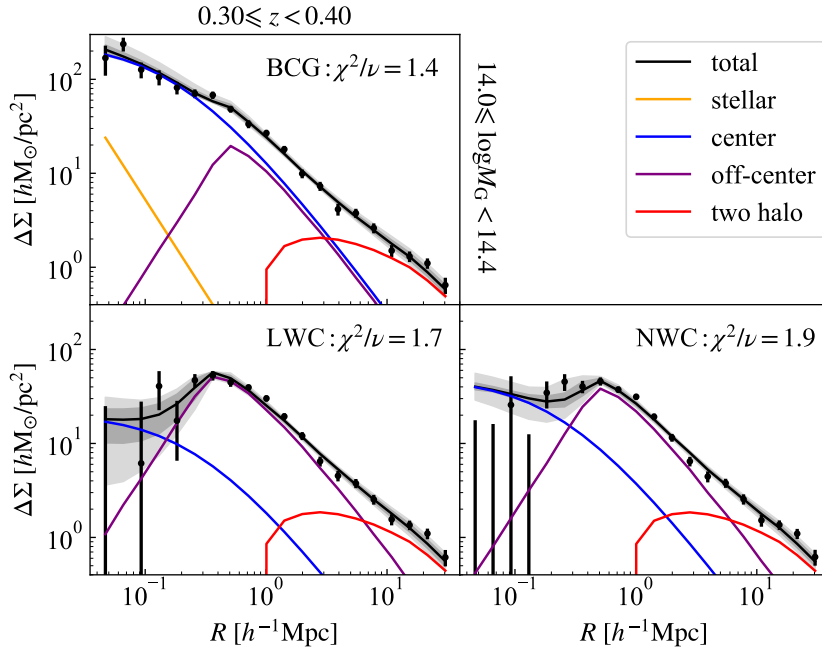


**Figure 3.** The best-fit results and different model components for lens sample with mass  $14.0 \leq \log M_G < 14.4$  at redshift  $0.3 \leq z < 0.4$ . The dark and light grey shaded regions represent the 68 and 95 confidence intervals of the total ESD fitting results, respectively. The three panels correspond to the three different type of group centers. The different colored lines represent the halo components labelled in the legend. The  $\chi^2/\nu$  value is also provided in each panel. Note here the degrees of freedom has a value of  $\nu = 15$ .

we take the set of parameters with the least  $\chi^2$  value as the best-fit results. The confidence regions of these parameters are obtained from their marginalized distributions.

For those who are interested in the whole list of parameters, we provide in the upper part of Table 1 with the best-fit parameters for all the 35 lens samples in different mass and redshift bins. For simplicity, here we only provide the best-fit parameters and  $\chi^2$  values for the BCG group centers. As an illustration, in each panel of Fig. 2 we show the best-fit model predictions of the ESD for the corresponding BCGs centroid lens sample as solid lines.

To be more specific, we show in Fig. 3 the best-fit results for a typical lens sample as shown in the center of Fig. 2, i.e., groups with mass  $14.0 \leq \log M_G < 14.4$  at redshift  $0.3 \leq z < 0.4$ . Here results are shown for three different types of group center as indicated in different panels. In each panel, the total and different ESD components as described in Eq. 7 are presented using different style lines. For all cases the four component model fits well on all scales. The stellar component contributes mainly at small scales for the BCG centroid (note that we do not include the stellar component for LWC and NWC centroids); the central term dominates on small

scales; the off-center term has relatively more impact on intermediate scales; and the two halo term dominates on large scales.

Fig. 4 shows the marginalized posterior distributions of the five parameters for ESDs in the above sample for the three group centers (see the bottom part of Table 1 for the detailed values of the best-fit parameters). The general properties of these five parameters are summarized below:

- The average halo mass,  $M_h$ , for each group centroid can be precisely measured at about 3-4% level, while the difference among different centroids is less than 5% level. Taking the statistical error and systematic difference into account, our halo mass estimation for this lens sample can achieve a precision at about 5% level.
- The concentrations  $c$  of the dark matter halos can also be well constrained and agree with each other among three centroids. Taking into account the significantly different ESD behaviors at small scales, the nice agreement of  $c$  is not trivial and can be regarded as a demonstration of the self-consistency of our model constraints. For the BCG case, we also see that the concentration  $c$  is some-



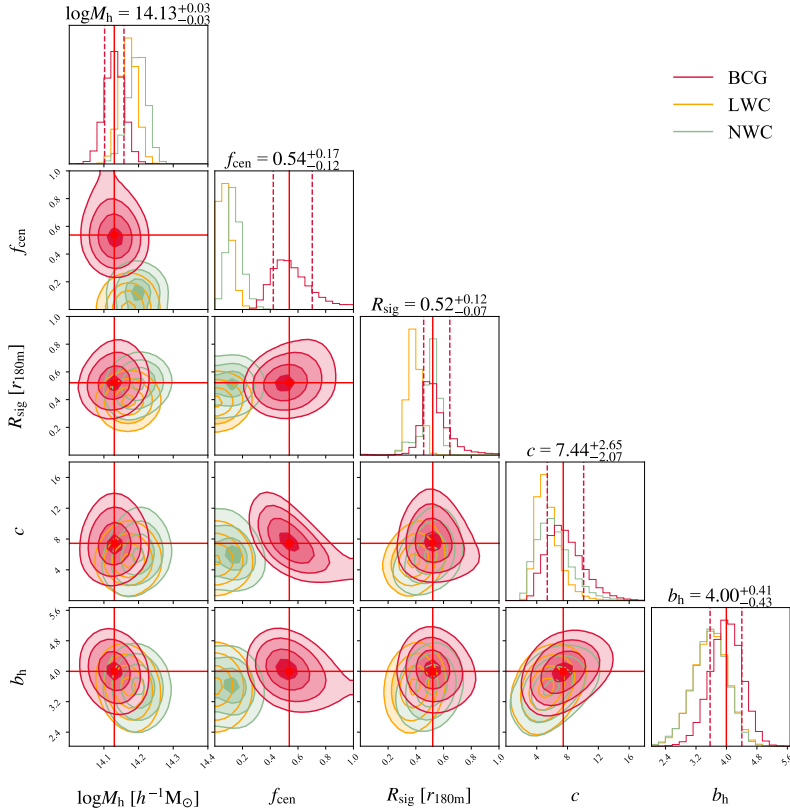


**Figure 4.** An example of marginalized posterior distributions of the five parameters  $\log M_h$ ,  $R_{\text{sig}}$ ,  $f_{\text{cen}}$ ,  $c$  and  $b_h$  for the lens sample with mass  $14.0 \leq \log M_G < 14.4$  at redshift  $0.3 \leq z < 0.4$ . Here the red, orange and green contours show the result for BCG, LWC, NWC centroids, respectively. The red solid lines show the best-fit result for the BCG sample. The red dashed lines show the  $1\text{-}\sigma$  confidence interval.

- what degenerate with  $f_{\text{cen}}$ , where a smaller  $c$  is associated with a larger  $f_{\text{cen}}$ .
- The  $b_h$  of the three centroids agrees with each other well within the  $1\text{-}\sigma$  error bar. This agreement is not surprising, as the ESDs at large scales are almost the same for these three group centroids.
  - Within those five free parameters, we see the center fraction  $f_{\text{cen}}$  has the biggest difference among the three different group centroids. The BCG centroid has a  $f_{\text{cen}} \sim 0.55$  and the LWC and NWC centroid have much lower  $f_{\text{cen}}$  values. Thus, overall, BCG is the best tracer of the halo center. Interestingly, such behavior is in good agreement with the related probes in literature (e.g. Skibba et al. 2011; Wang et al. 2014; Lange et al. 2018). For instance, by comparing the diffused X-ray peak positions and the most massive galaxies (MMGs) in the groups, Wang et al. (2014) found that  $\sim 65\%$  MMGs are located at the X-ray peak positions.

- Although the center fraction  $f_{\text{cen}}$  for different group centroids are quite different, the off-center parameters  $R_{\text{sig}}$  are not that different among these schemes. And it is also quite evident that Rayleigh distribution can nicely describe the off-centering effect, in its ability to reproduce the subtle ESD features at small scales, as shown in Fig. 3.

According to the above inspections, we can see that the mass, concentration and bias of the halos obtained from the three different centroid schemes are in good agreement with each other. Furthermore, the difference seen in the  $f_{\text{cen}}$  parameters for the three different centroid schemes is also theoretically expected (e.g. Skibba et al. 2011; Wang et al. 2014; Lange et al. 2018). Thus we believe that the main halo properties we obtain from our ESD measurements should be quite reliable.

#### 4. HALO PROPERTIES

Having demonstrated that the model parameters can be reliably constrained using the ESD measurements, we proceed to discuss the halo properties we extracted. As different group centers may impact the  $f_{\text{cen}}$  and  $R_{\text{sig}}$  parameters, we focus only on the other three parameters

**Table 1.** Posterior of parameters we obtained from the ESDs of our 35 lens samples (upper part) and the 20th lens sample with three types of group centers (lower part). In the upper part, we only list the posterior for the BCG group centers. In the bottom part, we list the results of all three centroids for sample 20, shown in Fig. 3. The redshift/mass range refers to the redshift/log of prior group mass used in the bin. The following five columns  $\log M_h$ ,  $c$ ,  $b_h$ ,  $f_{\text{cen}}$  and  $R_{\text{sig}}$  are the posterior of the parameters obtained from the MCMC chains. The upper and lower  $1\text{-}\sigma$  errors are given using the superscript and subscript, respectively. We also give the  $\chi^2/\nu$  showing the fitting quality for each sample (here the degree of freedom of the system is either 14 or 15, depending on the redshift bin used (see Section 3.1)).

Sample	mass range	redshift range	$\log M_h$	$f_{\text{cen}}$	$R_{\text{sig}}$	$c$	$b_h$	$\chi^2/\nu$
1	[13.00,13.20)	[0.10,0.20)	$13.28^{+0.03}_{-0.03}$	$0.53^{+0.10}_{-0.07}$	$0.50^{+0.07}_{-0.06}$	$14.86^{+2.95}_{-3.81}$	$1.84^{+0.20}_{-0.20}$	1.10
2	[13.20,13.40)	[0.10,0.20)	$13.44^{+0.05}_{-0.05}$	$0.67^{+0.20}_{-0.17}$	$0.68^{+0.33}_{-0.25}$	$7.25^{+3.37}_{-2.08}$	$1.48^{+0.24}_{-0.24}$	1.05
3	[13.40,13.60)	[0.10,0.20)	$13.70^{+0.04}_{-0.04}$	$0.43^{+0.12}_{-0.08}$	$0.53^{+0.08}_{-0.06}$	$11.78^{+3.86}_{-3.71}$	$1.30^{+0.31}_{-0.32}$	1.41
4	[13.60,13.80)	[0.10,0.20)	$13.86^{+0.05}_{-0.05}$	$0.62^{+0.23}_{-0.17}$	$0.64^{+0.30}_{-0.18}$	$6.42^{+3.66}_{-2.13}$	$1.95^{+0.43}_{-0.44}$	1.80
5	[13.80,14.00)	[0.10,0.20)	$14.12^{+0.04}_{-0.04}$	$0.32^{+0.05}_{-0.04}$	$0.67^{+0.05}_{-0.04}$	$13.31^{+1.50}_{-1.94}$	$2.36^{+0.51}_{-0.50}$	1.45
6	[14.00,14.40)	[0.10,0.20)	$14.27^{+0.06}_{-0.05}$	$0.72^{+0.19}_{-0.17}$	$0.88^{+0.48}_{-0.45}$	$4.01^{+1.68}_{-1.02}$	$2.22^{+0.69}_{-0.68}$	1.71
7	[14.40,15.00)	[0.10,0.20)	$14.71^{+0.04}_{-0.05}$	$0.35^{+0.07}_{-0.05}$	$0.90^{+0.12}_{-0.08}$	$9.09^{+1.65}_{-1.99}$	$3.73^{+1.08}_{-1.09}$	2.01
8	[13.00,13.20)	[0.20,0.30)	$13.15^{+0.04}_{-0.04}$	$0.50^{+0.11}_{-0.07}$	$0.54^{+0.12}_{-0.08}$	$13.33^{+3.59}_{-3.55}$	$1.73^{+0.12}_{-0.12}$	1.97
9	[13.20,13.40)	[0.20,0.30)	$13.37^{+0.03}_{-0.03}$	$0.40^{+0.06}_{-0.04}$	$0.52^{+0.05}_{-0.04}$	$16.27^{+2.01}_{-3.18}$	$1.56^{+0.14}_{-0.14}$	2.73
10	[13.40,13.60)	[0.20,0.30)	$13.49^{+0.04}_{-0.04}$	$0.62^{+0.16}_{-0.12}$	$0.75^{+0.22}_{-0.21}$	$7.88^{+2.79}_{-2.18}$	$1.78^{+0.18}_{-0.19}$	1.80
11	[13.60,13.80)	[0.20,0.30)	$13.72^{+0.04}_{-0.04}$	$0.64^{+0.18}_{-0.14}$	$0.59^{+0.19}_{-0.23}$	$7.59^{+2.63}_{-2.01}$	$2.25^{+0.25}_{-0.25}$	2.52
12	[13.80,14.00)	[0.20,0.30)	$13.90^{+0.03}_{-0.03}$	$0.50^{+0.14}_{-0.10}$	$0.56^{+0.15}_{-0.07}$	$9.44^{+3.30}_{-2.53}$	$2.34^{+0.30}_{-0.31}$	1.62
13	[14.00,14.40)	[0.20,0.30)	$14.20^{+0.03}_{-0.03}$	$0.48^{+0.08}_{-0.07}$	$0.78^{+0.06}_{-0.06}$	$9.11^{+1.91}_{-1.76}$	$3.65^{+0.34}_{-0.35}$	1.89
14	[14.40,15.00)	[0.20,0.30)	$14.58^{+0.04}_{-0.04}$	$0.74^{+0.18}_{-0.18}$	$0.69^{+0.60}_{-0.27}$	$3.44^{+1.36}_{-0.78}$	$5.01^{+0.96}_{-1.04}$	1.47
15	[13.00,13.20)	[0.30,0.40)	$13.15^{+0.04}_{-0.04}$	$0.60^{+0.11}_{-0.08}$	$0.75^{+0.14}_{-0.13}$	$10.90^{+2.18}_{-2.26}$	$1.67^{+0.11}_{-0.11}$	1.46
16	[13.20,13.40)	[0.30,0.40)	$13.37^{+0.04}_{-0.04}$	$0.52^{+0.14}_{-0.09}$	$0.65^{+0.09}_{-0.08}$	$9.73^{+2.71}_{-2.73}$	$1.77^{+0.14}_{-0.14}$	1.21
17	[13.40,13.60)	[0.30,0.40)	$13.51^{+0.03}_{-0.04}$	$0.48^{+0.12}_{-0.08}$	$0.66^{+0.11}_{-0.09}$	$10.05^{+2.79}_{-2.75}$	$2.01^{+0.18}_{-0.19}$	1.57
18	[13.60,13.80)	[0.30,0.40)	$13.70^{+0.04}_{-0.04}$	$0.66^{+0.20}_{-0.17}$	$0.67^{+0.41}_{-0.22}$	$5.41^{+2.46}_{-1.44}$	$2.38^{+0.25}_{-0.24}$	2.29
19	[13.80,14.00)	[0.30,0.40)	$13.84^{+0.05}_{-0.05}$	$0.59^{+0.18}_{-0.13}$	$0.79^{+0.27}_{-0.21}$	$7.26^{+2.71}_{-2.17}$	$2.93^{+0.31}_{-0.31}$	1.86
20	[14.00,14.40)	[0.30,0.40)	$14.13^{+0.03}_{-0.03}$	$0.54^{+0.17}_{-0.12}$	$0.52^{+0.12}_{-0.07}$	$7.44^{+2.65}_{-2.07}$	$3.81^{+0.39}_{-0.41}$	1.38
21	[14.40,15.00)	[0.30,0.40)	$14.59^{+0.04}_{-0.04}$	$0.47^{+0.16}_{-0.10}$	$0.62^{+0.12}_{-0.11}$	$6.01^{+2.49}_{-1.89}$	$6.07^{+1.02}_{-1.10}$	1.45
22	[13.00,13.20)	[0.40,0.50)	$13.07^{+0.04}_{-0.04}$	$0.58^{+0.15}_{-0.10}$	$0.55^{+0.14}_{-0.08}$	$12.82^{+3.89}_{-4.59}$	$1.74^{+0.12}_{-0.12}$	2.45
23	[13.20,13.40)	[0.40,0.50)	$13.26^{+0.05}_{-0.05}$	$0.67^{+0.15}_{-0.11}$	$0.80^{+0.18}_{-0.19}$	$9.29^{+2.30}_{-2.46}$	$2.00^{+0.16}_{-0.16}$	2.66
24	[13.40,13.60)	[0.40,0.50)	$13.44^{+0.05}_{-0.05}$	$0.57^{+0.22}_{-0.13}$	$0.73^{+0.28}_{-0.19}$	$7.31^{+3.56}_{-2.82}$	$1.95^{+0.19}_{-0.20}$	1.48
25	[13.60,13.80)	[0.40,0.50)	$13.61^{+0.04}_{-0.05}$	$0.48^{+0.14}_{-0.09}$	$0.63^{+0.13}_{-0.10}$	$10.34^{+3.08}_{-3.21}$	$2.56^{+0.25}_{-0.25}$	2.24
26	[13.80,14.00)	[0.40,0.50)	$13.77^{+0.05}_{-0.04}$	$0.63^{+0.21}_{-0.16}$	$0.48^{+0.51}_{-0.10}$	$9.55^{+5.76}_{-3.41}$	$2.97^{+0.38}_{-0.39}$	3.02
27	[14.00,14.40)	[0.40,0.50)	$14.13^{+0.03}_{-0.03}$	$0.51^{+0.21}_{-0.12}$	$0.63^{+0.13}_{-0.09}$	$7.78^{+3.80}_{-2.93}$	$4.20^{+0.49}_{-0.53}$	1.29
28	[14.40,15.00)	[0.40,0.50)	$14.47^{+0.05}_{-0.04}$	$0.64^{+0.24}_{-0.23}$	$0.41^{+0.54}_{-0.17}$	$5.72^{+2.80}_{-1.47}$	$5.73^{+1.02}_{-1.05}$	1.64
29	[13.00,13.20)	[0.50,0.60)	$12.93^{+0.06}_{-0.06}$	$0.64^{+0.22}_{-0.23}$	$0.49^{+0.23}_{-0.29}$	$10.17^{+4.72}_{-3.47}$	$1.60^{+0.16}_{-0.17}$	1.45
30	[13.20,13.40)	[0.50,0.60)	$13.18^{+0.07}_{-0.06}$	$0.60^{+0.21}_{-0.16}$	$0.63^{+0.36}_{-0.21}$	$8.82^{+4.40}_{-3.07}$	$1.92^{+0.20}_{-0.20}$	1.82
31	[13.40,13.60)	[0.50,0.60)	$13.41^{+0.06}_{-0.06}$	$0.70^{+0.18}_{-0.17}$	$0.72^{+0.44}_{-0.36}$	$7.38^{+3.37}_{-2.14}$	$2.19^{+0.24}_{-0.25}$	1.26
32	[13.60,13.80)	[0.50,0.60)	$13.59^{+0.06}_{-0.06}$	$0.27^{+0.10}_{-0.08}$	$0.54^{+0.09}_{-0.08}$	$12.97^{+3.64}_{-3.93}$	$2.61^{+0.31}_{-0.31}$	1.85
33	[13.80,14.00)	[0.50,0.60)	$13.65^{+0.06}_{-0.06}$	$0.25^{+0.36}_{-0.16}$	$0.28^{+0.10}_{-0.07}$	$9.25^{+6.01}_{-4.19}$	$3.40^{+0.47}_{-0.50}$	1.05
34	[14.00,14.40)	[0.50,0.60)	$14.15^{+0.04}_{-0.04}$	$0.41^{+0.12}_{-0.07}$	$0.65^{+0.09}_{-0.06}$	$11.53^{+2.87}_{-3.70}$	$3.85^{+0.60}_{-0.63}$	2.31
35	[14.40,15.00)	[0.50,0.60)	$14.59^{+0.09}_{-0.09}$	$0.60^{+0.24}_{-0.20}$	$1.09^{+1.03}_{-0.35}$	$4.07^{+3.14}_{-1.56}$	$3.65^{+1.66}_{-1.46}$	0.65
20 - BCG	[14.00,14.40)	[0.30,0.40)	$14.13^{+0.03}_{-0.03}$	$0.54^{+0.17}_{-0.12}$	$0.52^{+0.12}_{-0.07}$	$7.44^{+2.65}_{-2.07}$	$3.81^{+0.39}_{-0.41}$	1.38
20 - LWC	[14.00,14.40)	[0.30,0.40)	$14.17^{+0.02}_{-0.02}$	$0.07^{+0.05}_{-0.04}$	$0.39^{+0.05}_{-0.04}$	$5.21^{+1.75}_{-1.17}$	$3.42^{+0.42}_{-0.45}$	1.66
20 - NWC	[14.00,14.40)	[0.30,0.40)	$14.20^{+0.03}_{-0.03}$	$0.14^{+0.06}_{-0.05}$	$0.51^{+0.05}_{-0.06}$	$5.97^{+2.44}_{-1.90}$	$3.42^{+0.41}_{-0.45}$	1.89

obtained from the BCG centroid schemes. For the readers who are interested in the actual differences among the three group centroid schemes, we include a discussion in the Appendix B (Fig. 8).

#### 4.1. Comparing the halo mass and group mass

As we can see from the likelihood distribution of parameters in Fig. 4, we can have fairly good constraints on the halo bias, concentration and mass of our lens samples. It would be interesting to have a direct comparison between the halo masses obtained from the ESD fittings and the group masses provided by the group catalog. As the group mass obtained in Y21 is based on the halo abundance matching method, it in general refers to the abundance of the groups. Provided that the cosmologies are correct, the group mass should not have systematical biases.

In the upper row of Fig. 5, we compare the best-fit halo masses obtained from the weak lensing signals and the mean group masses obtained from the abundance matching method. The two agree with each other very well in the redshift range  $0.2 \leq z < 0.4$ , but are systematically different at lower and higher redshift bins. In the lowest redshift bin, the group masses are systematically smaller than the halo masses, while in the two highest redshift bins, the group masses exceed the halo masses. According to Table 1, the halo masses obtained from the ESDs are higher/lower than those obtained from the group catalog by about 0.1~0.2 dex in the lowest/highest redshift bins. This discrepancy is discussed in more detail with the help of cumulative halo mass functions in Section 5.1.

#### 4.2. Concentration - halo mass relation

In the middle row of Fig. 5, we show the concentration of our lens samples as a function of halo mass. Although the error bars are somewhat large, there is a clear trend that the concentration decreases with the halo mass.

For comparison, we also show in each panel the model predictions of Zhao et al. (2009); Dutton & Macciò (2014); Diemer & Joyce (2019) under the Planck18 cosmology in the related redshift bin. The corresponding results are shown as the solid, dashed and dot-dashed lines, respectively. Here we have properly converted their halo mass definition into ours, i.e., halos are defined to have 180 times the mean background density, using the COLOSSUS package (Diemer 2018). Overall, our observational constraints are somewhat higher than the model predictions, especially in the high redshift bins. Due to the large error bars, the mild redshift dependence presented in these theoretical models can not be verified.

In Fig.6 we also provide a comparison of concentration measurements with the data recently obtained by Ingegria et al. (2022, hereafter I22) from the ESDs around the AMICO clusters. Note that the cosmology adopted in that work is somewhat different from ours, i.e. a flat  $\Lambda$ CDM model with  $\Omega_m = 0.3$ ,  $\Omega_b = 0.05$ ,  $h = 0.7$  and the  $\sigma_8$  they constrained is  $0.63^{+0.11}_{-0.10}$ . The results are shown in the upper panels of Fig. 6. Since I22 has less redshift bins, we only show our results in the middle three redshift bins and compare them with the closest redshift bins. In each panel, we show the theoretical predictions from Zhao et al. (2009) for Planck18 (solid curves) as well as the cosmology obtained by I22 (dashed lines). The two different sets of cosmology lead to slight differences in the theoretical predictions. Overall, our results seems to have a better quality than that of I22. But there is no indication for a systematic difference between our concentration measurement and those of I22.

#### 4.3. Bias - halo mass relation

In the lowest panels of Fig. 5, we show the halo biases of our 35 lens samples as functions of the halo mass. For comparisons, in each redshift bin, we also show the theoretical model predictions of Jing et al. (1998); Sheth et al. (2001); Seljak & Warren (2004); Tinker et al. (2010), presented using solid, dashed, dot-dashed, and dotted lines respectively. Again, we have properly converted their halo mass definition into ours. Within these theoretical predictions, Seljak & Warren (2004) model has the strongest halo mass and redshift evolution dependence under the Planck18 cosmology. The other three models, although with slightly different amplitudes, have very similar dependence on the halo mass and redshift.

Our observational measurements of the halo biases have a good agreement with these theoretical model predictions, except for the lowest redshift bin. Overall, our observational data favor the model predictions of Jing et al. (1998); Sheth et al. (2001); Tinker et al. (2010). The biases in the lowest redshift bin are slightly lower than the theoretical predictions. However, due to the large error bars in this bin, the deviation is only at about 1-2  $\sigma$  level. Nevertheless, it is still worthwhile to check its significance and origin, either from the lensing signal measurements or the cosmological perspectives, which we will carry out in a separate paper.

We also provide a comparison of our bias measurements with two sets of very recent observational constraints in the bottom panels of Fig. 6. The first set of bias measurements are obtained by Sun et al. (2022, hereafter S22) from the cross-correlation between the DESI groups and the CMB lensing signals. The other

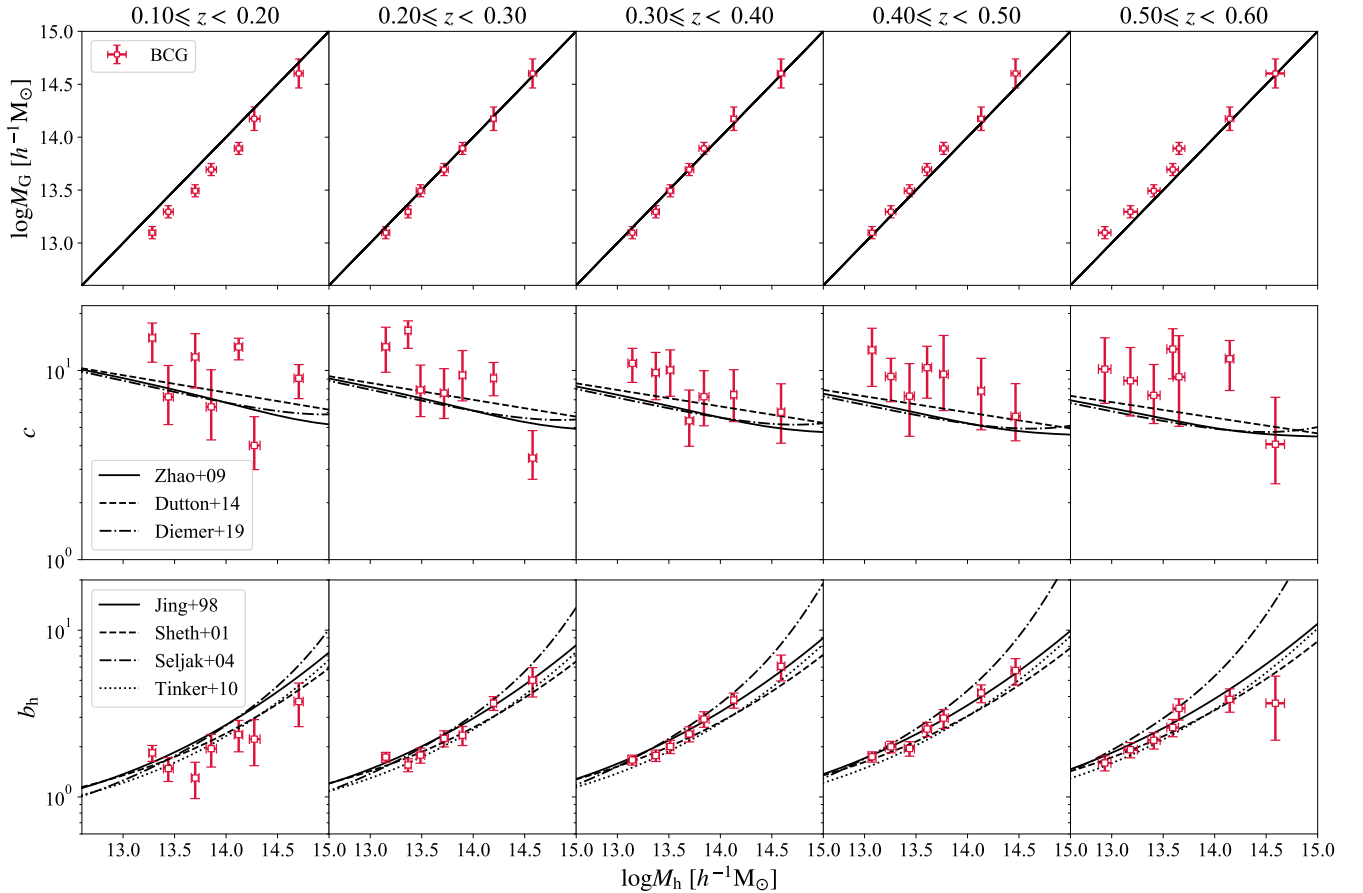


**Figure 5.** This plot shows the halo properties measured from the ESDs of our 35 lens samples. Shown in different columns are results for lens samples in different redshift bins as indicated on top of each column. The  $x$ -axis is the halo mass measured from weak lensing. The data points in each panel show the best-fit value for the BCG centroid schemes. (a) Shown in the top row panels are the comparisons between the lensing halo mass ( $\log M_h$ ) v.s. the group mass estimated using the abundance matching method ( $\log M_G$ ). Note that the error along the  $y$ -axis is the standard error of the group mass of the sample, while the error along the  $x$ -axis indicate the  $1\text{-}\sigma$  confidence interval of the fitting. The black lines are the reference lines where  $\log M_G = \log M_h$ . (b) The middle row panels show the concentration-mass relation measured from the ESDs. The  $y$ -axis is the halo concentration. The theoretical predictions of the  $c$ - $M$  relations from Zhao et al. (2009); Dutton & Macciò (2014); Diemer & Joyce (2019) are shown as the solid, dashed and dashdot lines, respectively. (c) The bottom row panels show the halo bias-mass relations. The theoretical predictions of the  $b$ - $M$  relations from Jing et al. (1998); Sheth et al. (2001); Seljak & Warren (2004); Tinker et al. (2010) are shown as the solid, dashed, dashdot and dotted lines, respectively.

set of bias measurements are obtained by I22. The results are shown in different symbols. In each panel, we only show the theoretical predictions from Jing et al. (1998) at the average redshift of our sample under the Planck 18 cosmology (solid curves) as well as the cosmological model obtained by I22 (dashed curves), as reference. The results obtained by S22 is in rough agreement with our measurements. On the other hand, the results of I22 are somewhat lower than our bias measurements in the two higher redshift bins. Their error bars are larger due to their much smaller lens sample sizes.

## 5. CUMULATIVE HALO MASS FUNCTIONS

In Fig.7, we show the cumulative halo mass functions (CHMFs) in five redshift bins obtained directly from

the group catalog (the black dashed lines) and those from weak lensing measurement (the red points), and compare them to the theoretical predictions (the black solid lines). In deriving the CHMFs, we have properly taken into account the completeness and purity corrections from the group catalog in Y21, as well as a halo mass correction due to the mass scatter in the weak lensing measurement. In the rest of this section, we give some details regarding our data processing, and discuss about some of our limitations.

### 5.1. CHMFs adopted in the group catalog

For each of the redshift bins, we count the total number of groups that are more massive than a given group mass,  $N_G(> M_G)$ . While in calculating this number, we

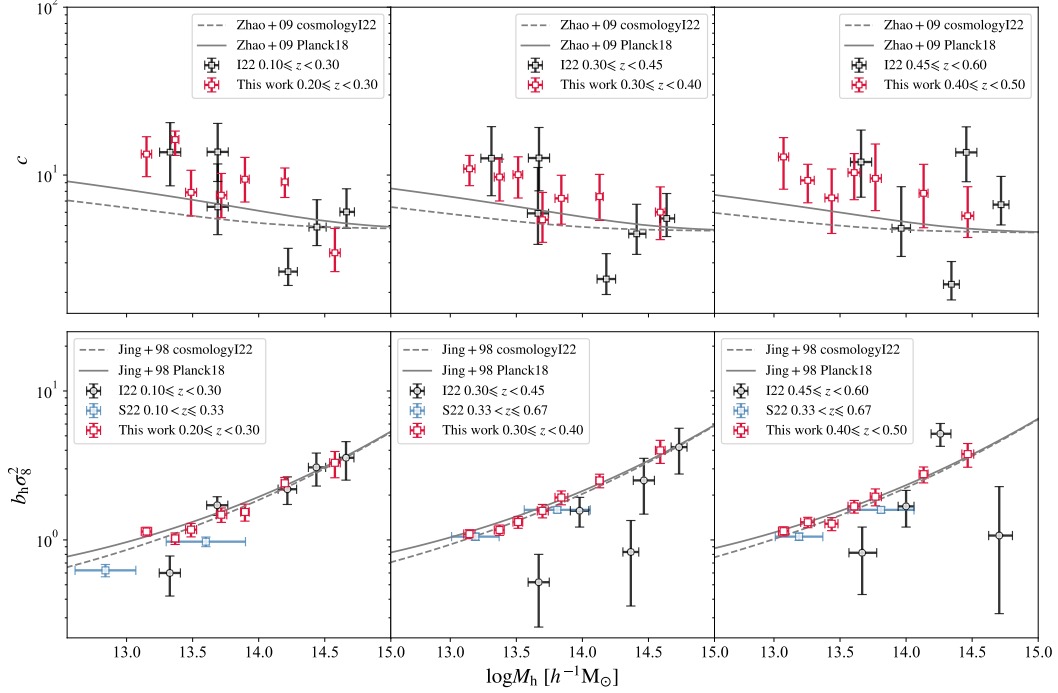


**Figure 6.** We compare our concentration and bias measurements to previous observations by [Ingolia et al. \(2022\)](#) and [Sun et al. \(2022\)](#) using different types of symbols, with average redshift of each sample within  $0.2 \leq z < 0.6$ . Here we only show the results in three redshift bin within  $0.2 \leq z < 0.5$ . We present the theoretical predictions under Planck18 cosmology in solid lines and the one under the cosmology obtained in I22 in dashed lines.

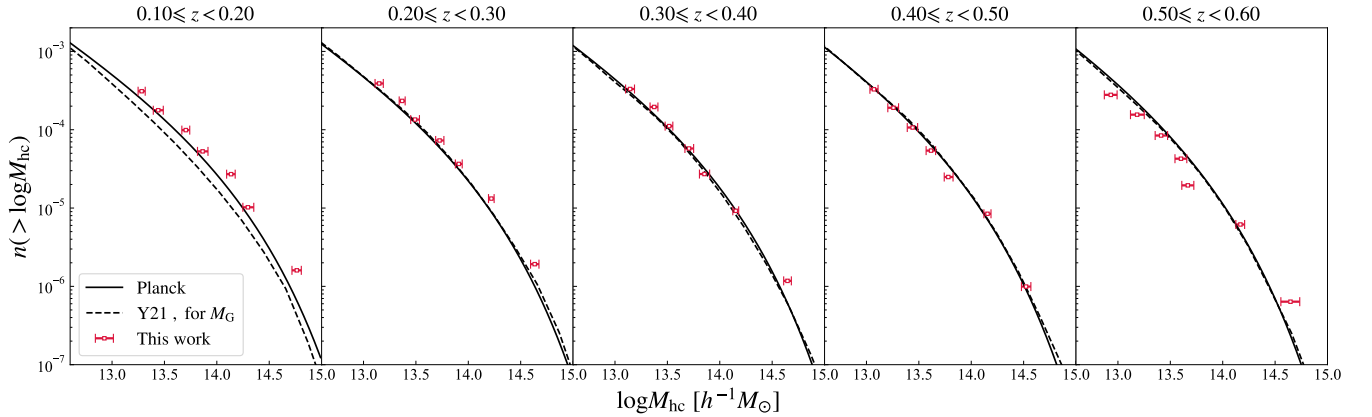


**Figure 7.** The cumulative halo mass functions (CHMFs) in five different redshift bins. The red points with error bars show the CHMFs obtained from the weak lensing ESD measurements. The black dashed lines show the CHMFs obtained from the group catalog of [Yang et al. \(2021\)](#) with the correction using Eq. 14. The black solid lines show the theoretical CHMFs using fitting functions from [Tinker et al. \(2008\)](#) under the Planck18 cosmology ([Planck Collaboration et al. 2020](#)).

have properly taken into account the completeness and purity of the groups as obtained by Y21 from the mock DESI redshift galaxy and group samples,

$$N_G(> M_G) = \sum_i^{M_{G,i} > M_G} f_{\text{group}}(M_{G,i}) / f_{\text{halo}}(M_{G,i}), \quad (14)$$

where  $f_{\text{halo}}$  and  $f_{\text{group}}$  are the completeness and purity of the groups (see Fig. 8 of Y21), respectively. Here  $M_{G,i}$  is the mass of the  $i$ -th group in the whole catalog, after ranking according to their masses. Note that since the group masses,  $M_G$ , provided in Y21 group catalog were assigned based on abundance matching to the halo mass functions assuming the Planck18 cosmology, these masses are cosmology dependent. However, even if a dif-

**Table 2.** The values of cumulative halo mass function measured in this work (plotted as the red points in Fig. 7). There are seven data points in each redshift bin, provided within two columns: halo mass and the number density of halos with mass larger than this halo mass.

ID	$0.1 \leq z < 0.2$		$0.2 \leq z < 0.3$		$0.3 \leq z < 0.4$		$0.4 \leq z < 0.5$		$0.5 \leq z < 0.6$	
	$\log M_{\text{hc}}$	$n(> M_{\text{hc}})$	$\log M_{\text{hc}}$	$n(> M_{\text{hc}})$	$\log M_{\text{hc}}$	$n(> M_{\text{hc}})$	$\log M_{\text{hc}}$	$n(> M_{\text{hc}})$	$\log M_{\text{hc}}$	$n(> M_{\text{hc}})$
	$h^{-1}M_{\odot}$	$(\times 10^{-5})$	$h^{-1}M_{\odot}$	$(\times 10^{-5})$	$h^{-1}M_{\odot}$	$(\times 10^{-5})$	$h^{-1}M_{\odot}$	$(\times 10^{-5})$	$h^{-1}M_{\odot}$	$(\times 10^{-5})$
1	$13.28^{+0.03}_{-0.03}$	31.0	$13.15^{+0.04}_{-0.04}$	39.0	$13.14^{+0.04}_{-0.04}$	33.1	$13.07^{+0.04}_{-0.04}$	32.8	$12.93^{+0.06}_{-0.06}$	27.9
2	$13.44^{+0.05}_{-0.05}$	17.7	$13.37^{+0.03}_{-0.03}$	23.3	$13.37^{+0.04}_{-0.04}$	19.5	$13.26^{+0.05}_{-0.05}$	19.1	$13.18^{+0.07}_{-0.06}$	15.6
3	$13.70^{+0.04}_{-0.04}$	9.89	$13.49^{+0.04}_{-0.04}$	13.5	$13.52^{+0.03}_{-0.04}$	11.1	$13.44^{+0.05}_{-0.05}$	10.7	$13.41^{+0.06}_{-0.06}$	8.43
4	$13.86^{+0.05}_{-0.05}$	5.29	$13.73^{+0.04}_{-0.04}$	7.29	$13.71^{+0.04}_{-0.04}$	5.76	$13.62^{+0.04}_{-0.05}$	5.41	$13.60^{+0.06}_{-0.06}$	4.27
5	$14.14^{+0.04}_{-0.04}$	2.71	$13.91^{+0.03}_{-0.03}$	3.66	$13.85^{+0.05}_{-0.05}$	2.72	$13.78^{+0.05}_{-0.04}$	2.49	$13.67^{+0.06}_{-0.06}$	1.95
6	$14.30^{+0.06}_{-0.05}$	1.02	$14.22^{+0.03}_{-0.03}$	1.32	$14.15^{+0.03}_{-0.03}$	0.922	$14.16^{+0.03}_{-0.03}$	0.845	$14.17^{+0.04}_{-0.04}$	0.617
7	$14.76^{+0.04}_{-0.05}$	0.160	$14.63^{+0.04}_{-0.04}$	0.192	$14.65^{+0.04}_{-0.04}$	0.118	$14.52^{+0.05}_{-0.04}$	0.0994	$14.65^{+0.09}_{-0.09}$	0.0637

ferent cosmology had been used to assign group masses, and  $M_G$  would be different, their rank-order would be preserved. Thus the ranked number of groups is cosmology independent.

Once we obtained the total number of groups  $N_G(> M_G)$  that are more massive than  $M_G$ , we can normalize it according to the volume of each lens sample, and thus get the cumulative number density of the groups,  $n_G(> M_G)$ , which are shown in Fig. 7 as black dashed lines. Note that, in this step, since we need cosmological parameters, especially  $\Omega_m$ , to calculate the comoving volume, it is also cosmology dependent. Here again, we adopt the parameters from the Planck18 cosmology for our distance calculation.

Ideally, as the group masses,  $M_G$ , were assigned according to the Planck18 cosmology, the dashed line in each panel of Fig. 7 should agree with the theoretical prediction described by the solid line. However, we find that in the lowest redshift bin with  $0.1 \leq z < 0.2$ , it is somewhat lower than the expectation. This discrepancy indicates that the group abundance within this redshift bin is somewhat underestimated due to some systematic effects, such as redshift errors. Upon this feature, we are able to explain the discrepancy between the group mass and lensing mass shown in Fig. 5 with the following four main possible reasons: (1) the abundance of the groups is not consistent with Planck18 prediction in the lowest redshift bin, which was induced by different redshift bin widths that are used for group ranking (0.1 in this study v.s. 0.33 in Y21), (2) the Planck18 cosmology assumed in Y21 is incorrect, (3) there are systematic error in the halo masses inferred from the ESDs, and (4) the rank-order according to total group luminosity is not equal to rank-order in actual halo mass.

### 5.2. CHMFs obtained from the weak lensing measurements

As we have obtained the measurements of the halo masses for each of our 35 lens samples, with a typical uncertainty at 4-13% level (see Table 1), it would be straightforward to measure the CHMFs. Dong et al. (2019, hereafter D19) pointed out that, the weak lensing mass measurement can nicely recover the cumulative halo mass functions (CHMFs) when the groups are ranked and binned using a mass proxy. Our choice for the mass proxy in this work is obviously the group mass  $M_G$  of Y21. For each of the 35 lens samples, we define  $\hat{M}_G$  as its mean mass, and use  $n_G(> \hat{M}_G)$  obtained in §5.1 to denote the halo abundance that the sample corresponds to. We can then use the weak lensing mass,  $M_h$ , of each sample to replace  $\hat{M}_G$  to form the CHMFs from weak lensing.

However, as pointed out in D19, the halo mass scatter induced by the mass proxy can lead to a bias in the average halo mass of a mass bin. Due to the shape of the halo mass function, there are more contaminations from the lower mass end than those from the higher end, causing the lensing mass to be slightly lower than the ideal case. The cumulative halo mass function obtained from the weak lensing signals is therefore slightly impacted by the mass scatter, especially at the massive end (see Fig. 1 of D19). To correct for such an effect, we use a Monte Carlo method to obtain a mass correction factor,  $\Delta \log M$ , and define the final lensing mass,  $M_{\text{hc}}$ , with  $\log M_{\text{hc}} = \log M_h + \Delta \log M$ . The details regarding the derivation of  $\Delta \log M$  are outlined in Appendix C.

We shown in Fig. 7 the CHMFs in the five redshift bins, obtained from our lensing measurement on 35 lens samples in red dots with error bars. Here since the abundance of the lens systems are rather deterministic, we neglect the error bars along the  $y$ -axis. We provide the values of our measurements in Table 2.

### 5.3. Discussion

Compare to the Planck18 model predictions, our observational measurements agree with the model predictions quite well in the intermediate three redshift bins, and are slightly higher and lower in the lowest and highest redshift bins, respectively. This discrepancy may be caused by either some possible systematics that our current ESD measurements haven't properly taken into account or the cosmology that we adopted is not the most appropriate one. Apart from these, although the weak lensing ESD measurements can provide us direct estimations of the true underlying halo masses, some systematics can also be brought on by effects including asphericity, miscentering, dynamical state, photometric redshift uncertainties, halo member contamination, uncorrelated LSS, assumed density model, and the mass dispersion within the mass bin, etc. (King & Schneider 2001; Becker & Kravtsov 2011; Oguri & Hamana 2011; Bahé et al. 2012; Han et al. 2015; Henson et al. 2017; Lee et al. 2018; Fong et al. 2019; Grandis et al. 2021). Here we have taken into account some of the major effects, e.g., photometric redshift uncertainties, miscentering and mass dispersion. However, all the other effects may slightly impact our CHMF results as well. We will come back to this topic by combining weak lensing data from other observations in a forthcoming paper.

Finally, we note that, as the halo masses we obtained from the weak lensing signals are relatively independent of the cosmology we assumed, except ESD signals somehow rely on  $\Omega_m$  (see More 2013, for related discussions), we can use the group mass v.s. halo mass relations shown in the upper panels of Fig. 5 to calibrate/update the group masses in Y21 group catalog. We believe the updated group masses should be less dependent on the assumption of Planck18 cosmology, at least, e.g., the  $\sigma_8$  value.

## 6. CONCLUSIONS

In this study, based on the DESI Legacy Imaging Surveys DR9, we probed the dark matter halo properties of 35 lens samples, ranging in redshifts  $0.1 \leq z < 0.6$  and group masses  $10^{13}-10^{15} h^{-1} M_\odot$ . The 35 lens samples are selected from the group catalogs constructed by Y21 using an extended halo-based group finder. To quantify the halo information, we make use of the weak lensing shear catalogs from the high quality DECaLS data using the Fourier\_Quad method.

We measured the weak lensing signals (ESDs) of these 35 lens samples for three group centroid schemes: the brightest central galaxy (BCG), the luminosity weighted center (LWC) and the number weighted center (NWC), respectively. We take into account the central fraction, off-centering effect and the two halo term contributions

in our ESD model to constrain the halo properties for all the lens samples. Our main findings are summarized below:

- The ESD model can nicely describe the very different subtle features in the observational ESD measurements among different group centroids over a wide scale range. The best-fit halo masses, concentrations and biases are self-consistent among different choices of the centroids.
- The off-center component in our ESD model nicely reproduces the off-centering effects at small scales, and can distinguish different center indicators with their very different amounts of center fractions  $f_{\text{cen}}$ .
- The halo masses we obtained from the ESDs are slightly different from those provided by Y21 based on the abundance matching method discrepancy can be attributed to a small systematic in the group abundance estimation in the lowest redshift bin, systematic errors in the halo mass estimations from the ESD measurements, or the cosmology used to estimate the halo mass.
- The concentration - halo mass relations obtained for different redshift bins and halo mass ranges are somewhat higher than the theoretical predictions. Unfortunately, the precision of the measurements is insufficient to test the prediction that halos of a given mass are less concentrated at higher redshifts.
- The bias - halo mass relations are obtained and also in good agreement with most of the theoretical predictions, except for the lowest redshift bin, in which the observational data prefers slightly lower biases.
- By properly taking into account the halo completeness and group purity in the group finding algorithm of Y21, we obtain the number density of groups above the average group mass in each redshift bin. This in turn provides us measurements of the cumulative halo mass functions down to  $M_h \sim 10^{13} h^{-1} M_\odot$  in five redshift bins, that are free from the Eddington bias.
- Finally, for those who are interested in our data, we have provided the halo properties we extract from our 35 lens samples in Table 1, and the cumulative halo mass function measurements in Table 2.

Our method and results open up new avenues for group/cluster cosmology, provided that stacked weak lensing signals can be accurately measured from high quality imaging surveys and reliable and complete halo systems can be detected from the foreground large (spectroscopic or photometric) redshift galaxy surveys. As we mentioned earlier, these measurements hold important information regarding the cosmology and structure formation information, we will come to this topic in a forthcoming paper.

We sincerely thank the anonymous referee for helpful comments that significantly improved the presentation of this paper. This work is supported by the National Key Basic Research and Development Program of China (No.2018YFA0404504, 2021YFC2203100), the national science foundation of China (Nos. 11833005, 11890691, 11890692, 11621303, 12073017, 12192224), 111 project No.B20019, and Shanghai Natural Science Foundation, grant No. 19ZR1466800. We acknowledge the science research grants from the China Manned Space Project with Nos. CMS-CSST-2021-A02, CMS-CSST-2021-A01. F.Y.D. is supported by a KIAS Individual Grant PG079001 at Korea Institute for Advanced Study. The computations in this paper were run on the  $\pi$ 2.0 cluster supported by the Center for High Performance Computing and the Gravity Supercomputer at Shanghai Jiao Tong University.

The Legacy Imaging Surveys of the DESI footprint is supported by the Director, Office of Science, Office of High Energy Physics of the U.S. Department of Energy under Contract No. DE-AC02-05CH1123, by the National Energy Research Scientific Computing Center, a DOE Office of Science User Facility under the same contract; and by the U.S. National Science Foundation, Division of Astronomical Sciences under Contract No. AST-0950945 to NOAO. The Photometric Redshifts for the Legacy Surveys (PRLS) catalog used in this paper was produced thanks to funding from the U.S. Department of Energy Office of Science, Office of High Energy Physics via grant DE-SC0007914.

## REFERENCES

- Bacon, D. J., & Taylor, A. N. 2003, *MNRAS*, 344, 1307, doi: [10.1046/j.1365-8711.2003.06922.x](https://doi.org/10.1046/j.1365-8711.2003.06922.x)
- Bahé, Y. M., McCarthy, I. G., & King, L. J. 2012, *MNRAS*, 421, 1073, doi: [10.1111/j.1365-2966.2011.20364.x](https://doi.org/10.1111/j.1365-2966.2011.20364.x)
- Bartelmann, M., & Schneider, P. 2001, *PhR*, 340, 291, doi: [10.1016/S0370-1573\(00\)00082-X](https://doi.org/10.1016/S0370-1573(00)00082-X)
- Becker, M. R., & Kravtsov, A. V. 2011, *ApJ*, 740, 25, doi: [10.1088/0004-637X/740/1/25](https://doi.org/10.1088/0004-637X/740/1/25)
- Bernstein, G. M., & Armstrong, R. 2014, *MNRAS*, 438, 1880, doi: [10.1093/mnras/stt2326](https://doi.org/10.1093/mnras/stt2326)
- Bernstein, G. M., & Jarvis, M. 2002, *AJ*, 123, 583, doi: [10.1086/338085](https://doi.org/10.1086/338085)



- Bertin, E., & Arnouts, S. 1996, *A&AS*, 117, 393, doi: [10.1051/aas:1996164](https://doi.org/10.1051/aas:1996164)
- Biviano, A., Murante, G., Borgani, S., et al. 2006, *A&A*, 456, 23, doi: [10.1051/0004-6361:20064918](https://doi.org/10.1051/0004-6361:20064918)
- Blanton, M. R., & Roweis, S. 2007, *AJ*, 133, 734, doi: [10.1086/510127](https://doi.org/10.1086/510127)
- Bridle, S. L., Kneib, J. P., Bardeau, S., & Gull, S. F. 2002, in *The Shapes of Galaxies and their Dark Halos*, ed. P. Natarajan, 38–46, doi: [10.1142/9789812778017\\_0006](https://doi.org/10.1142/9789812778017_0006)
- Davis, M., Efstathiou, G., Frenk, C. S., & White, S. D. M. 1985, *ApJ*, 292, 371, doi: [10.1086/163168](https://doi.org/10.1086/163168)
- Dey, A., Schlegel, D. J., Lang, D., et al. 2019, *AJ*, 157, 168, doi: [10.3847/1538-3881/ab089d](https://doi.org/10.3847/1538-3881/ab089d)
- Diemer, B. 2018, *ApJS*, 239, 35, doi: [10.3847/1538-4365/aaee8c](https://doi.org/10.3847/1538-4365/aaee8c)
- Diemer, B., & Joyce, M. 2019, *ApJ*, 871, 168, doi: [10.3847/1538-4357/aafad6](https://doi.org/10.3847/1538-4357/aafad6)
- Dong, F., Zhang, J., Yang, X., Zhang, J., & Luo, W. 2019, *ApJ*, 883, 155, doi: [10.3847/1538-4357/ab3a9d](https://doi.org/10.3847/1538-4357/ab3a9d)
- Du, W., Fan, Z., Shan, H., et al. 2015, *ApJ*, 814, 120, doi: [10.1088/0004-637X/814/2/120](https://doi.org/10.1088/0004-637X/814/2/120)
- Dutton, A. A., & Macciò, A. V. 2014, *MNRAS*, 441, 3359, doi: [10.1093/mnras/stu742](https://doi.org/10.1093/mnras/stu742)
- Elahi, P. J., Power, C., Lagos, C. d. P., Poulton, R., & Robotham, A. S. G. 2018, *MNRAS*, 477, 616, doi: [10.1093/mnras/sty590](https://doi.org/10.1093/mnras/sty590)
- Erben, T., Hildebrandt, H., Miller, L., et al. 2013, *MNRAS*, 433, 2545, doi: [10.1093/mnras/stt928](https://doi.org/10.1093/mnras/stt928)
- Fong, M., Choi, M., Catlett, V., et al. 2019, *MNRAS*, 488, 3340, doi: [10.1093/mnras/stz1882](https://doi.org/10.1093/mnras/stz1882)
- Fong, M., Han, J., Zhang, J., et al. 2022, *Monthly Notices of the Royal Astronomical Society*, doi: [10.1093/mnras/stac1263](https://doi.org/10.1093/mnras/stac1263)
- Foreman-Mackey, D., Hogg, D. W., Lang, D., & Goodman, J. 2013, *Publications of the Astronomical Society of the Pacific*, 125, 306–312, doi: [10.1086/670067](https://doi.org/10.1086/670067)
- Fujita, Y., & Aung, H. 2019, *ApJ*, 875, 26, doi: [10.3847/1538-4357/ab0e02](https://doi.org/10.3847/1538-4357/ab0e02)
- Gao, L., Springel, V., & White, S. D. M. 2005, *MNRAS*, 363, L66, doi: [10.1111/j.1745-3933.2005.00084.x](https://doi.org/10.1111/j.1745-3933.2005.00084.x)
- Gao, L., & White, S. D. M. 2007, *MNRAS*, 377, L5, doi: [10.1111/j.1745-3933.2007.00292.x](https://doi.org/10.1111/j.1745-3933.2007.00292.x)
- George, M. R., Leauthaud, A., Bundy, K., et al. 2012, *ApJ*, 757, 2, doi: [10.1088/0004-637X/757/1/2](https://doi.org/10.1088/0004-637X/757/1/2)
- Grandis, S., Bocquet, S., Mohr, J. J., Klein, M., & Dolag, K. 2021, *MNRAS*, 507, 5671, doi: [10.1093/mnras/stab2414](https://doi.org/10.1093/mnras/stab2414)
- Gruen, D., Seitz, S., Brimiouille, F., et al. 2014, *Monthly Notices of the Royal Astronomical Society*, 442, 1507, doi: [10.1093/mnras/stu949](https://doi.org/10.1093/mnras/stu949)
- Han, J., Eke, V. R., Frenk, C. S., et al. 2015, *MNRAS*, 446, 1356, doi: [10.1093/mnras/stu2178](https://doi.org/10.1093/mnras/stu2178)
- Henson, M. A., Barnes, D. J., Kay, S. T., McCarthy, I. G., & Schaye, J. 2017, *MNRAS*, 465, 3361, doi: [10.1093/mnras/stw2899](https://doi.org/10.1093/mnras/stw2899)
- Heymans, C., Brown, M. L., Barden, M., et al. 2005, *MNRAS*, 361, 160, doi: [10.1111/j.1365-2966.2005.09152.x](https://doi.org/10.1111/j.1365-2966.2005.09152.x)
- Heymans, C., van Waerbeke, L., Miller, L., et al. 2012, *Monthly Notices of the Royal Astronomical Society*, 427, 146, doi: [10.1111/j.1365-2966.2012.21952.x](https://doi.org/10.1111/j.1365-2966.2012.21952.x)
- Hirata, C., & Seljak, U. 2003, *MNRAS*, 343, 459, doi: [10.1046/j.1365-8711.2003.06683.x](https://doi.org/10.1046/j.1365-8711.2003.06683.x)
- Hoekstra, H., Herbonnet, R., Muzzin, A., et al. 2015, *Monthly Notices of the Royal Astronomical Society*, 449, 685, doi: [10.1093/mnras/stv275](https://doi.org/10.1093/mnras/stv275)
- Ingolia, L., Covone, G., Sereno, M., et al. 2022, *Monthly Notices of the Royal Astronomical Society*, 511, 1484, doi: [10.1093/mnras/stac046](https://doi.org/10.1093/mnras/stac046)
- Jing, Y. P. 2000, *ApJ*, 535, 30, doi: [10.1086/308809](https://doi.org/10.1086/308809)
- Jing, Y. P., Mo, H. J., & Börner, G. 1998, *ApJ*, 494, 1, doi: [10.1086/305209](https://doi.org/10.1086/305209)
- Johnston, D. E., Sheldon, E. S., Wechsler, R. H., et al. 2007, arXiv e-prints, arXiv:0709.1159, <https://arxiv.org/abs/0709.1159>
- Kaiser, N., Squires, G., & Broadhurst, T. 1995, *ApJ*, 449, 460, doi: [10.1086/176071](https://doi.org/10.1086/176071)
- King, L. J., & Schneider, P. 2001, *A&A*, 369, 1, doi: [10.1051/0004-6361:20010030](https://doi.org/10.1051/0004-6361:20010030)
- Kitching, T. D., Miller, L., Heymans, C. E., van Waerbeke, L., & Heavens, A. F. 2008, *MNRAS*, 390, 149, doi: [10.1111/j.1365-2966.2008.13628.x](https://doi.org/10.1111/j.1365-2966.2008.13628.x)
- Lacey, C., & Cole, S. 1993, *MNRAS*, 262, 627, doi: [10.1093/mnras/262.3.627](https://doi.org/10.1093/mnras/262.3.627)
- Lange, J. U., van den Bosch, F. C., Hearin, A., et al. 2018, *MNRAS*, 473, 2830, doi: [10.1093/mnras/stx2434](https://doi.org/10.1093/mnras/stx2434)
- Lange, J. U., van den Bosch, F. C., Zentner, A. R., Wang, K., & Villarreal, A. S. 2019, *MNRAS*, 487, 3112, doi: [10.1093/mnras/stz1466](https://doi.org/10.1093/mnras/stz1466)
- Lee, B. E., Le Brun, A. M. C., Haq, M. E., et al. 2018, *MNRAS*, 479, 890, doi: [10.1093/mnras/sty1377](https://doi.org/10.1093/mnras/sty1377)
- Li, H., Zhang, J., Liu, D., et al. 2021, *The Astrophysical Journal*, 908, 93, doi: [10.3847/1538-4357/abcda3](https://doi.org/10.3847/1538-4357/abcda3)
- Li, Q., Han, J., Wang, W., et al. 2021, *MNRAS*, 505, 3907, doi: [10.1093/mnras/stab1633](https://doi.org/10.1093/mnras/stab1633)
- Li, Z.-Z., Qian, Y.-Z., Han, J., Wang, W., & Jing, Y. P. 2019, *ApJ*, 886, 69, doi: [10.3847/1538-4357/ab4f6d](https://doi.org/10.3847/1538-4357/ab4f6d)
- Ludlow, A. D., Navarro, J. F., Boylan-Kolchin, M., et al. 2013, *MNRAS*, 432, 1103, doi: [10.1093/mnras/stt526](https://doi.org/10.1093/mnras/stt526)
- Luo, W., Yang, X., Zhang, J., et al. 2017, *ApJ*, 836, 38, doi: [10.3847/1538-4357/836/1/38](https://doi.org/10.3847/1538-4357/836/1/38)

- Luo, W., Yang, X., Lu, T., et al. 2018, *The Astrophysical Journal*, 862, 4
- Mandelbaum, R., Seljak, U., Kauffmann, G., Hirata, C. M., & Brinkmann, J. 2006, *MNRAS*, 368, 715, doi: [10.1111/j.1365-2966.2006.10156.x](https://doi.org/10.1111/j.1365-2966.2006.10156.x)
- Mandelbaum, R., Hirata, C. M., Seljak, U., et al. 2005, *MNRAS*, 361, 1287, doi: [10.1111/j.1365-2966.2005.09282.x](https://doi.org/10.1111/j.1365-2966.2005.09282.x)
- Mandelbaum, R., Rowe, B., Armstrong, R., et al. 2015, *Monthly Notices of the Royal Astronomical Society*, 450, 2963, doi: [10.1093/mnras/stv781](https://doi.org/10.1093/mnras/stv781)
- Maoli, R., Mellier, Y., van Waerbeke, L., et al. 2000, *The Messenger*, 101, 10
- McGaugh, S. S., & van Dokkum, P. 2021, *Research Notes of the American Astronomical Society*, 5, 23, doi: [10.3847/2515-5172/abelba](https://doi.org/10.3847/2515-5172/abelba)
- Medezinski, E., Battaglia, N., Umetsu, K., et al. 2017, *Publications of the Astronomical Society of Japan*, 70, doi: [10.1093/pasj/psx128](https://doi.org/10.1093/pasj/psx128)
- Miller, L., Kitching, T. D., Heymans, C., Heavens, A. F., & van Waerbeke, L. 2007, *MNRAS*, 382, 315, doi: [10.1111/j.1365-2966.2007.12363.x](https://doi.org/10.1111/j.1365-2966.2007.12363.x)
- More, S. 2013, *The Astrophysical Journal*, 777, L26, doi: [10.1088/2041-8205/777/2/L26](https://doi.org/10.1088/2041-8205/777/2/L26)
- Munari, E., Biviano, A., Borgani, S., Murante, G., & Fabjan, D. 2013, *MNRAS*, 430, 2638, doi: [10.1093/mnras/stt049](https://doi.org/10.1093/mnras/stt049)
- Oguri, M., & Hamana, T. 2011, *MNRAS*, 414, 1851, doi: [10.1111/j.1365-2966.2011.18481.x](https://doi.org/10.1111/j.1365-2966.2011.18481.x)
- Penna-Lima, M., Bartlett, J. G., Rozo, E., et al. 2017, *Astronomy & Astrophysics*, 604, A89, doi: [10.1051/0004-6361/201629971](https://doi.org/10.1051/0004-6361/201629971)
- Planck Collaboration, Aghanim, N., Akrami, Y., et al. 2020, *A&A*, 641, A6, doi: [10.1051/0004-6361/201833910](https://doi.org/10.1051/0004-6361/201833910)
- Prada, F., Klypin, A. A., Cuesta, A. J., Betancort-Rijo, J. E., & Primack, J. 2012, *MNRAS*, 423, 3018, doi: [10.1111/j.1365-2966.2012.21007.x](https://doi.org/10.1111/j.1365-2966.2012.21007.x)
- Prada, F., Klypin, A. A., Simonneau, E., et al. 2006, *ApJ*, 645, 1001, doi: [10.1086/504456](https://doi.org/10.1086/504456)
- Pratt, G. W., Croston, J. H., Arnaud, M., & Böhringer, H. 2009, *A&A*, 498, 361, doi: [10.1051/0004-6361/200810994](https://doi.org/10.1051/0004-6361/200810994)
- Press, W. H., & Schechter, P. 1974, *ApJ*, 193, 437, doi: [10.1086/153179](https://doi.org/10.1086/153179)
- Refregier, A. 2003, *ARA&A*, 41, 645, doi: [10.1146/annurev.astro.41.111302.102207](https://doi.org/10.1146/annurev.astro.41.111302.102207)
- Rhodes, J., Refregier, A., & Groth, E. J. 2000, *ApJ*, 536, 79, doi: [10.1086/308902](https://doi.org/10.1086/308902)
- Schneider, P. 2005, arXiv e-prints, astro, <https://arxiv.org/abs/astro-ph/0509252>
- Seljak, U., & Warren, M. S. 2004, *MNRAS*, 355, 129, doi: [10.1111/j.1365-2966.2004.08297.x](https://doi.org/10.1111/j.1365-2966.2004.08297.x)
- Sereno, M., Covone, G., Izzo, L., et al. 2017, *Monthly Notices of the Royal Astronomical Society*, 472, 1946, doi: [10.1093/mnras/stx2085](https://doi.org/10.1093/mnras/stx2085)
- Sheth, R. K., Mo, H. J., & Tormen, G. 2001, *MNRAS*, 323, 1, doi: [10.1046/j.1365-8711.2001.04006.x](https://doi.org/10.1046/j.1365-8711.2001.04006.x)
- Skibba, R. A., van den Bosch, F. C., Yang, X., et al. 2011, *MNRAS*, 410, 417, doi: [10.1111/j.1365-2966.2010.17452.x](https://doi.org/10.1111/j.1365-2966.2010.17452.x)
- Smith, G. P., Mazzotta, P., Okabe, N., et al. 2015, *Monthly Notices of the Royal Astronomical Society: Letters*, 456, L74, doi: [10.1093/mnrasl/slv175](https://doi.org/10.1093/mnrasl/slv175)
- Smith, R. E., Peacock, J. A., Jenkins, A., et al. 2003, *MNRAS*, 341, 1311, doi: [10.1046/j.1365-8711.2003.06503.x](https://doi.org/10.1046/j.1365-8711.2003.06503.x)
- Sun, Z., Yao, J., Dong, F., et al. 2022, *MNRAS*, 511, 3548, doi: [10.1093/mnras/stac138](https://doi.org/10.1093/mnras/stac138)
- Sunyaev, R. A., & Zeldovich, Y. B. 1972, *Comments on Astrophysics and Space Physics*, 4, 173
- Tasitsiomi, A., Kravtsov, A. V., Gottlöber, S., & Klypin, A. A. 2004, *ApJ*, 607, 125, doi: [10.1086/383219](https://doi.org/10.1086/383219)
- Tinker, J., Kravtsov, A. V., Klypin, A., et al. 2008, *ApJ*, 688, 709, doi: [10.1086/591439](https://doi.org/10.1086/591439)
- Tinker, J. L., Robertson, B. E., Kravtsov, A. V., et al. 2010, *ApJ*, 724, 878, doi: [10.1088/0004-637X/724/2/878](https://doi.org/10.1088/0004-637X/724/2/878)
- Tinker, J. L., Weinberg, D. H., Zheng, Z., & Zehavi, I. 2005, *ApJ*, 631, 41, doi: [10.1086/432084](https://doi.org/10.1086/432084)
- van den Bosch, F. C., More, S., Cacciato, M., Mo, H., & Yang, X. 2013, *MNRAS*, 430, 725, doi: [10.1093/mnras/sts006](https://doi.org/10.1093/mnras/sts006)
- van den Bosch, F. C., Norberg, P., Mo, H. J., & Yang, X. 2004, *MNRAS*, 352, 1302, doi: [10.1111/j.1365-2966.2004.08021.x](https://doi.org/10.1111/j.1365-2966.2004.08021.x)
- Van Waerbeke, L., Mellier, Y., Radovich, M., et al. 2001, *A&A*, 374, 757, doi: [10.1051/0004-6361:20010766](https://doi.org/10.1051/0004-6361:20010766)
- von der Linden, A., Mantz, A., Allen, S. W., et al. 2014, *Monthly Notices of the Royal Astronomical Society*, 443, 1973, doi: [10.1093/mnras/stu1423](https://doi.org/10.1093/mnras/stu1423)
- Wang, H., Zhang, J., Li, H., & Shen, Z. 2021, *The Astrophysical Journal*, 911, 10, doi: [10.3847/1538-4357/abe856](https://doi.org/10.3847/1538-4357/abe856)
- Wang, L., Yang, X., Shen, S., et al. 2014, *MNRAS*, 439, 611, doi: [10.1093/mnras/stt2481](https://doi.org/10.1093/mnras/stt2481)
- Wang, Y., Yang, X., Mo, H. J., van den Bosch, F. C., & Chu, Y. 2004, *MNRAS*, 353, 287, doi: [10.1111/j.1365-2966.2004.08141.x](https://doi.org/10.1111/j.1365-2966.2004.08141.x)
- Wechsler, R. H., Bullock, J. S., Primack, J. R., Kravtsov, A. V., & Dekel, A. 2002, *ApJ*, 568, 52, doi: [10.1086/338765](https://doi.org/10.1086/338765)

- White, S. D. M., Efstathiou, G., & Frenk, C. S. 1993, MNRAS, 262, 1023, doi: [10.1093/mnras/262.4.1023](https://doi.org/10.1093/mnras/262.4.1023)
- Xu, W., Shan, H., Li, R., et al. 2021, The Astrophysical Journal, 922, 162, doi: [10.3847/1538-4357/ac1b9e](https://doi.org/10.3847/1538-4357/ac1b9e)
- Xu, X., Zehavi, I., & Contreras, S. 2021, Monthly Notices of the Royal Astronomical Society, 502, 3242, doi: [10.1093/mnras/stab100](https://doi.org/10.1093/mnras/stab100)
- Yang, T., Cai, Y.-C., Cui, W., et al. 2022, arXiv e-prints, arXiv:2202.11430. <https://arxiv.org/abs/2202.11430>
- Yang, X., Mo, H. J., van den Bosch, F. C., & Jing, Y. P. 2005, MNRAS, 356, 1293, doi: [10.1111/j.1365-2966.2005.08560.x](https://doi.org/10.1111/j.1365-2966.2005.08560.x)
- Yang, X., Mo, H. J., van den Bosch, F. C., et al. 2006, MNRAS, 373, 1159, doi: [10.1111/j.1365-2966.2006.11091.x](https://doi.org/10.1111/j.1365-2966.2006.11091.x)
- Yang, X., Mo, H. J., van den Bosch, F. C., et al. 2007, The Astrophysical Journal, 671, 153, doi: [10.1086/522027](https://doi.org/10.1086/522027)
- Yang, X., Mo, H. J., van den Bosch, F. C., Zhang, Y., & Han, J. 2012, ApJ, 752, 41, doi: [10.1088/0004-637X/752/1/41](https://doi.org/10.1088/0004-637X/752/1/41)
- Yang, X., Xu, H., He, M., et al. 2021, ApJ, 909, 143, doi: [10.3847/1538-4357/abddb2](https://doi.org/10.3847/1538-4357/abddb2)
- Zhang, J. 2008, Monthly Notices of the Royal Astronomical Society, 383, 113, doi: [10.1111/j.1365-2966.2007.12585.x](https://doi.org/10.1111/j.1365-2966.2007.12585.x)
- Zhang, J. 2010, MNRAS, 403, 673, doi: [10.1111/j.1365-2966.2009.16168.x](https://doi.org/10.1111/j.1365-2966.2009.16168.x)
- Zhang, J. 2011, Journal of Cosmology and Astroparticle Physics, 2011, 041, doi: [10.1088/1475-7516/2011/11/041](https://doi.org/10.1088/1475-7516/2011/11/041)
- Zhang, J. 2016, National Science Review, 3, 159, doi: [10.1093/nsr/nww017](https://doi.org/10.1093/nsr/nww017)
- Zhang, J., Liu, C., Alonso Vaquero, P., et al. 2022, arXiv e-prints, arXiv:2206.02434. <https://arxiv.org/abs/2206.02434>
- Zhang, J., Luo, W., & Foucaud, S. 2015, Journal of Cosmology and Astroparticle Physics, 2015, 024, doi: [10.1088/1475-7516/2015/01/024](https://doi.org/10.1088/1475-7516/2015/01/024)
- Zhang, J., Zhang, P., & Luo, W. 2017, ApJ, 834, 8, doi: [10.3847/1538-4357/834/1/8](https://doi.org/10.3847/1538-4357/834/1/8)
- Zhang, J., Dong, F., Li, H., et al. 2019, ApJ, 875, 48, doi: [10.3847/1538-4357/ab1080](https://doi.org/10.3847/1538-4357/ab1080)
- Zhao, D. H., Jing, Y. P., Mo, H. J., & Börner, G. 2009, ApJ, 707, 354, doi: [10.1088/0004-637X/707/1/354](https://doi.org/10.1088/0004-637X/707/1/354)
- Zhou, R., Newman, J. A., Mao, Y.-Y., et al. 2021, MNRAS, 501, 3309, doi: [10.1093/mnras/staa3764](https://doi.org/10.1093/mnras/staa3764)
- Zou, H., Gao, J., Zhou, X., & Kong, X. 2019, ApJS, 242, 8, doi: [10.3847/1538-4365/ab1847](https://doi.org/10.3847/1538-4365/ab1847)
- Zu, Y., Mandelbaum, R., Simet, M., Rozo, E., & Rykoff, E. S. 2017, MNRAS, 470, 551, doi: [10.1093/mnras/stx1264](https://doi.org/10.1093/mnras/stx1264)
- Zu, Y., & Weinberg, D. H. 2013, MNRAS, 431, 3319, doi: [10.1093/mnras/stt411](https://doi.org/10.1093/mnras/stt411)
- Zu, Y., Weinberg, D. H., Jennings, E., Li, B., & Wyman, M. 2014, MNRAS, 445, 1885, doi: [10.1093/mnras/stu1739](https://doi.org/10.1093/mnras/stu1739)

## APPENDIX

## A. THE AVERAGE PROJECTED DENSITY OF THE HOST HALO

According to Yang et al. (2006), if the candidate lens galaxy (system) is located at the center of host halo, the average projected density of the host halo can be calculated from the NFW profile, where

$$\rho(r) = \frac{\rho_0}{(r/r_s)(1+r/r_s)^2}, \quad (\text{A1})$$

with  $\rho_0 = \frac{\bar{\rho}\Delta_{vir}}{3I}$ , where  $\Delta_{vir} = 180$ ,  $I = \frac{1}{c^3} \int_0^c \frac{xdx}{(1+x)^2}$ . Here  $c$  is the concentration parameter defined as the ratio between the virial radius of a halo and its characteristic scale radius  $r_s$ , with  $r_{180m} = c \times r_s$ . The projected surface density then can be analytically expressed as (Yang et al. 2006):

$$\Sigma_{\text{NFW}}(R) = \frac{M_h}{2\pi r_s^2 I} f(x), \quad (\text{A2})$$

where  $M_h$  is the halo mass and  $f(x)$  bears the following form with  $x = R/r_s$ :

$$f(x) = \begin{cases} \frac{1}{x^2-2} \left[ 1 - \frac{\ln \frac{1+\sqrt{1-x^2}}{x}}{\sqrt{1-x^2}} \right] & x < 1 \\ \frac{1}{3} & x = 1 \\ \frac{1}{x^2-1} \left[ 1 - \frac{\text{atan}(\frac{\sqrt{x^2-1}}{x})}{\sqrt{x^2-1}} \right] & x > 1. \end{cases} \quad (\text{A3})$$

On the other hand, if the candidate lens galaxy is not locate at the center of the host halo, but with an off-center distance  $R_{\text{off}}$ , the projected surface density will change from an NFW profile  $\Sigma_{\text{NFW}}(R)$  to

$$\Sigma_{\text{host}}(R|R_{\text{off}}) = \frac{1}{2\pi} \int_0^{2\pi} \Sigma_{\text{NFW}}(\sqrt{R^2 + R_{\text{off}}^2 + 2R_{\text{off}}R\cos\theta}) d\theta. \quad (\text{A4})$$

In the halo model, if we consider the mass or galaxy outside the host halo in consideration, which we call as the 2-halo term, we need to take into the halo exclusion effect Wang et al. (2004). Here we use the following function to describe this effect in the halo-matter cross correlation function,

$$f_{\text{exc}}(r) = \begin{cases} 0 & r < r_{180m} \\ 1 & \text{else.} \end{cases} \quad (\text{A5})$$

In addition to the halo exclusion effect, to accurately model the cross correlation functions at large scales, one needs to take into account the scale dependence of the halo bias,  $\zeta(r, z)$  (see Fong et al. (2022) for a more sophisticated treatment at this scale). Following van den Bosch et al. (2013), we start from the one obtained by Tinker et al. (2005), given by

$$\zeta_0(r, z) = \frac{[1 + 1.17 \xi_{\text{mm}}(r, z)]^{1.49}}{[1 + 0.69 \xi_{\text{mm}}(r, z)]^{2.09}}. \quad (\text{A6})$$

The subscript 0 indicates that this fitting function was calibrated for halos identified  $N$ -body simulations using the friends-of-friends (FOF) percolation algorithm (e.g. Davis et al. 1985), with a linking length of 0.2 times the mean interparticle separation. To take into account the diffidence between this and the one based on the spherical overdensity algorithm, van den Bosch et al. (2013) provided a modified version of the bias radial dependence function

$$\zeta(r, z) = \begin{cases} \zeta_0(r, z) & \text{if } r \geq r_\psi \\ \zeta_0(r_\psi, z) & \text{if } r < r_\psi \end{cases} \quad (\text{A7})$$

where the characteristic radius,  $r_\psi$ , is defined by

$$\log [\zeta_0(r_\psi, z) \xi_{\text{mm}}(r_\psi, z)] = \psi. \quad (\text{A8})$$

Here we adopt  $\psi = 0.9$ , the best chosen free parameter obtained in van den Bosch et al. (2013) for our investigation.

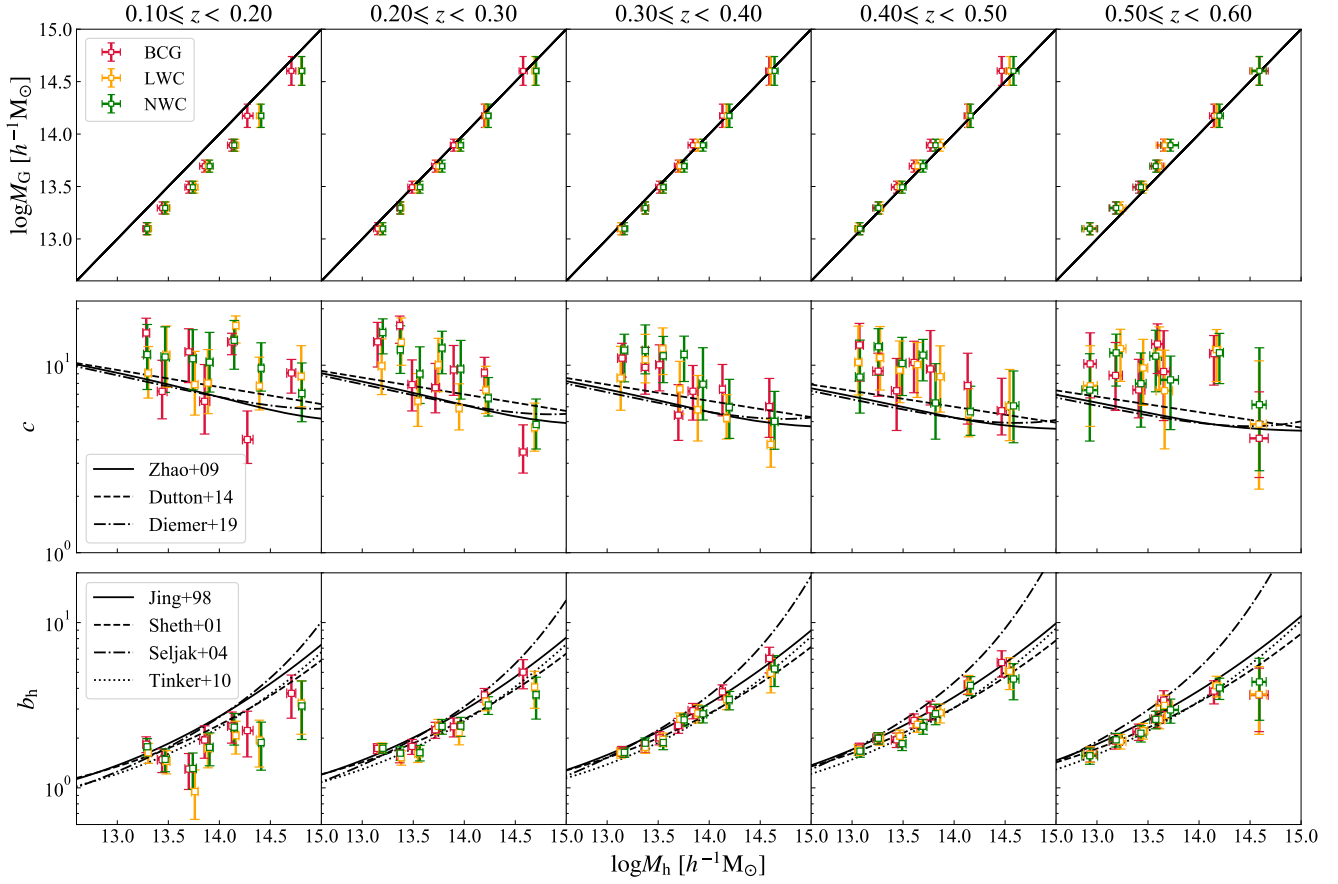


**Figure 8.** Similar as Fig. 5, but here for the three centroids separately. The red, orange, green points in each panel show the results obtained from signals using BCG, LWC, NWC as center indicators, respectively.

## B. THE DIFFERENCE AMONG THREE HALO CENTERING SCHEMES

Shown in Fig. 8 are the halo mass, concentration and bias ( $\log M_h$ ,  $c$  and  $b_h$ ) model constraints for our 35 lens samples in different redshift bins as indicated on top of each column separately. The red, orange, green points in each panel show the results obtained for the BCG, LWC, NWC centering schemes, respectively.

## C. MASS CORRECTION FACTOR ASSOCIATED WITH THE RANK-ORDER CHANGE

As pointed out in D19, a simple way to correct for or reduce the impact of the mass scatter to the measurements of the CHMFs is to add such a scatter into the lensing model, e.g. Eq. 7. However, adding such a scatter into Eq. 7 needs an additional level of integration, which is computationally very time consuming and quite impractical in this study. An alternative and less expensive way is to generate a set of Monte Carlo halos to mimic and correct for the impact of such an effect. We use the following procedures to make our correction:

- (1) We first generate a set of halos according to the halo mass function of Tinker et al. (2008) under the Planck18 cosmology, with true mass  $M_T$  ranging from  $10^{12}$  to  $10^{15} h^{-1} M_\odot$ . We can bin the halos according to the rank-order of their true mass and obtain the average mass  $\hat{M}_T \Big|_{\text{sorted-by-}M_T}$  inside each bin, which correspond to the corrected halo mass we desired to get.
- (2) Then, we add to each halo a log-normal scatter  $\Delta \log M_T$  according to the typical halo mass error in the group finder obtained by Y21 using mock data sets. Thus we obtain a scattered mass indicator  $\log M_O = \log M_T + \Delta \log M_T$ , where  $\Delta \log M_T$  is drawn from a log-normal distribution with a scatter varying from 0.3 dex ( $\sim 10^{11.6} h^{-1} M_\odot$ ), 0.4 dex ( $\sim 10^{12.3} h^{-1} M_\odot$ ) to 0.2 dex ( $\gtrsim 10^{14} h^{-1} M_\odot$ ) (see Fig. 9 of Y21). Here the rank-order of  $M_O$  resembles the rank-order of  $M_G$  in Y21.

- (3) Next, by the rank-order of  $M_O$ , we can bin the halos and obtain the average halo mass  $\hat{M}_T \Big|_{sorted-by-M_O}$ . In the ideal case where there are no systematic or random errors in the actual lensing measurements, this corresponds to the average halo mass  $M_h$  obtained from the lensing ESD measurement.
- (4) The mass difference between the rank-order by  $M_G$  and the true halo mass rank-order, which caused by the scatter we introduced, is thus  $\Delta \log M = \log \hat{M}_T \Big|_{sorted-by-M_T} - \log \hat{M}_T \Big|_{sorted-by-M_O}$ .

We use  $\Delta \log M$  in each bin to correct the lensing mass for the impact of scatter to our CHMF measurements. Its value ranges from almost zero in the low mass bins to 0.057 in the most massive bin.